Acta Pharmaceutica Sinica B 2025;15(10):4973−4994

Chinese Pharmaceutical Association
Institute of Materia Medica, Chinese Academy of Medical Sciences

Acta Pharmaceutica Sinica B

www.elsevier.com/locate/apsb
www.sciencedirect.com

ORIGINAL ARTICLE

# Self-illuminating liposome-derived *in situ* triggerable photodynamic therapy combining radionuclide therapy for synergistic treatment of lung cancer

**Chunsen Yuan[a,b,c,†], Taotao Jin[c,†], Hangke Lei[a,b,c,†], Juanjuan Liu[c], Wendan Pu[c], Yang Zhang[c], Chenwen Li[c,d,e], Dingde Huang[a,*], Jianxiang Zhang[c,d,e,*], Jiawei Guo[b,*]**

[a]*Department of Nuclear Medicine, Southwest Hospital, Third Military Medical University (Army Medical University), Chongqing 400038, China*
[b]*Department of Pharmaceutical Analysis, College of Pharmacy, Third Military Medical University (Army Medical University), Chongqing 400038, China*
[c]*Department of Pharmaceutics, College of Pharmacy, Third Military Medical University (Army Medical University), Chongqing 400038, China*
[d]*Yu-Yue Pathology Scientific Research Center, Chongqing 400039, China*
[e]*State Key Laboratory of Trauma and Chemical Poisoning, Third Military Medical University (Army Medical University), Chongqing 400038, China*

Received 29 January 2025; received in revised form 14 May 2025; accepted 20 May 2025

**KEY WORDS**

Lung cancer;
Photodynamic therapy;
Radiopharmaceutical;
Liposome;
Reactive oxygen species;
Antitumor

**Abstract** The persistent high prevalence and poor survival outcomes of lung cancer underscore the urgent need for innovative therapeutic modalities. Here, we present a novel multifunctional delivery platform for the synergistic treatment of lung malignancies, combining *in situ*-triggerable photodynamic therapy (PDT) with radiotherapy. The new platform CLL was developed by loading a new reactive oxygen species (ROS)-triggerable photosensitizer, luminol-conjugated chlorin e6 (Ce6), into liposomes. CLL can be activated through the bioluminescence resonance energy transfer effect under oxidative stress, thereby producing singlet oxygen for targeted tumor treatment without external irradiation. *In vitro* studies showed significant cytotoxic effects of CLL in both 4T1 and A549 tumor cells. Furthermore, a PDT-

This article is part of a special issue entitled: Targeted Radiopharmaceuticals published in Acta Pharmaceutica Sinica B.

*Corresponding authors.
E-mail addresses: huangdingde@126.com (Dingde Huang), jxzhang@tmmu.edu.cn (Jianxiang Zhang), breakhp@163.com (Jiawei Guo).
[†]These authors made equal contributions to this work.

Peer review under the responsibility of Chinese Pharmaceutical Association and Institute of Materia Medica, Chinese Academy of Medical Sciences.

https://doi.org/10.1016/j.apsb.2025.06.026

radiopharmaceutical combination nanotherapy CLL-$^{177}$Lu was engineered by incorporating the radionuclide $^{177}$Lu into CLL. CLL-$^{177}$Lu demonstrated synergistic antitumor effects in 4T1 and A549 tumor cells, as well as in mouse models of 4T1 breast cancer lung metastasis or A549 tumor xenografts. Mechanistically, CLL-$^{177}$Lu can induce singlet oxygen/ROS generation, enhance tumor cell apoptosis, and promote M1 macrophage-mediated immunotherapy. Preliminary assessments showed a favorable profile for CLL-$^{177}$Lu, highlighting its potential as a promising nanotherapy for cancer treatment. Additionally, CLL can serve as a versatile platform for delivering a range of therapies to achieve synergistic antitumor effects.



## 1. Introduction

Lung cancer persists as the predominant neoplasm worldwide, with high prevalence and mortality rates[1,2]. Despite advancement of conventional treatments, such as surgery, chemotherapy, and radiation therapy[3,4], the limited response rates and poor survival outcomes in lung cancer patients highlight the urgent need for novel and effective therapies[5-8]. In recent decades, photodynamic therapy (PDT) represents a revolutionary modality for cancer therapy due to its non-invasiveness, high space-time selectivity, limited susceptibility to drug resistance, and low-toxic side effects[9-11]. In the clinic, PDT has been successfully employed for the treatment of lung, esophageal, prostate, bladder, non-melanoma skin, and head and neck cancers[12,13]. However, conventional PDT regimens require laser irradiation and suffer from non-specific activation of photosensitizers[14,15]. Moreover, antitumor effects of PDT are depth-limited due to the constraints in light penetration within tissues[16]. Additionally, some patients experience photoallergic reactions that can impair the effectiveness and patient compliance[17].

In this regard, *in situ* triggerable PDT approaches employing self-luminescent materials as an internal irradiation source are promising for treating deep-seated tumors, without the need to consider the tissue penetration limitations and photoallergic drawbacks associated with conventional PDT strategies. Instead of relying on external activation, electronic excitations can be transferred to the photosensitizer molecules through chemiluminescence/bioluminescence resonance energy transfer (CRET/BRET), fluorescence resonance energy transfer, or Cherenkov radiation energy transfer[18]. The CRET/BRET effect is particularly appealing for developing the "auto-PDT" platform, which has emerged as a promising modality for PDT. Key components of CRET/BRET systems include suitable electronic donors and accepters, where donor molecules can be activated *in vivo* through biochemical reactions. This process enables the transfer of excited-state energy to photosensitizers for PDT activation without the need for external light. By leveraging these mechanisms, various combinations such as luciferase-luciferin Rose Bengal[19], $^{89}$Zr-chlorin e6 (Ce6)[20], RLuc8 protein-QD655-Ce6[14], luminol-$FeSO_4$-protoporphyrin IX[21], and Ce6-luminol[22], have been constructed in the form of nanoparticles and investigated in preclinical studies. In different animal models of cancers, these *in-situ* triggerable PDT nanotherapies have demonstrated promising antitumor activities. Of note, nanoplatforms were found beneficial for increasing the effectiveness of *in-situ* PDT regimens. Nevertheless, PDT alone displays considerable limitations in clinical treatments of cancers, mainly resulting from their complexity and heterogeneity[23-26]. Furthermore, the effectiveness of PDT is notably compromised in lung cancer patients with larger, peripheral, and advanced tumors. This limitation has heightened the urgent need to explore combination therapy strategies that integrate PDT with other intervention options to improve antitumor efficacy[27,28]. Rationally engineered combination therapies integrating *in-situ* PDT with other clinical treatment modalities are better positioned to afford desirable therapeutic effects.

Recently, the latest guidelines on PDT by the European Dermatology Forum and the British Association of Dermatologists have strongly recommended the integration of PDT with other therapeutic modalities, particularly for treating Bowen's disease and nodular basal cell carcinoma, based on compelling evidence of their efficacy[29]. Notably, clinical trials have demonstrated the superiority of ranibizumab in combination with PDT compared to ranibizumab alone for the treatment of polypoidal choroidal vasculopathy[30]. Also, pre-clinical studies have indicated that core−shell polymer nanoparticle-mediated PDT can significantly enhance therapeutic efficacy of anti-PD-L1 immune checkpoint blockers in a murine model of metastatic triple-negative breast cancer[31]. Additionally, M-SAO@$SiO_2$ nanoparticles, engineered by encapsulating a photosensitizer merocyanine 540 and a luminescent material $SrAl_2O_4$:$Eu^{2+}$ within mesoporous silica, showed significantly enhanced antitumor efficacy for X-ray treatment after combination with PDT[32]. Furthermore, Cherenkov-induced PDT combined with $^{68}$Ga, a PET imaging radionuclide, afforded synergistic antitumor activity in B16F10 cells *in vitro*. Promising tumoricidal effects were also found when PDT was combined with other therapeutic radionuclides, such as $^{90}$Y[33]. Despite the great potential of PDT combining chemotherapies, immune therapies, and radionuclide therapies in achieving synergistic antitumor effects, the majority of these PDT combinations have complicated structures based on non-degradable and/or non-biocompatible materials, leading to difficulties in cost-effective mass production and quality control as well as *in vivo* safety concerns from the viewpoint of clinical translation. Further, external irradiation sources are necessary for these PDT-based combination therapies.

On the other hand, recent clinical studies on the application of radionuclide therapies or PDT have highlighted the necessity of combination therapy. Notably, this combination can improve the overall health status in over 80% of patients and facilitate the initiation of radiotherapy[34-36]. When PDT is integrated with radiotherapy, it enhances tumor sensitivity to radiation, potentially reducing exposure time or the required radiation dose, while also generating reactive oxygen species (ROS) that boost antitumor efficacy[37-39]. Moreover, the combination of PDT with local

radiotherapy is effective in alleviating airway obstruction in patients[40,41]. Additionally, radionuclide therapies can augment therapeutic effects of PDT through Cherenkov radiation, mainly by addressing depth dependency and providing additional tumoricidal effects[33,42,43]. Notably, the $^{177}$Lu nuclide, a frequently utilized therapeutic metal nuclide in the clinic, exhibits optimal half-life of 6.65 days and a maximum energy of 498 keV, enabling tissue penetration over an average range of 670 μm[44,45]. Furthermore, $^{177}$Lu causes minimal damage to surrounding healthy tissues and exhibits a less impact on bone marrow following radiation in the target lesions. In 2018, the FDA approved $^{177}$Lu-DOTATATE for tumor therapy, which can be used for treating prostatic cancer, lung cancer and other malignancies[46]. However, some disadvantages of $^{177}$Lu-derived therapies remain to be addressed, such as short half-life in blood circulation, non-specific distribution in non-target organs, and short retention and poor accumulation in the tumor tissues[47], thus emphasizing the need for novel delivery strategies.

Herein, we report a novel multifunctional platform integrating PDT and a radionuclide for synergistically treating lung malignancies (Scheme 1). An *in situ* triggerable compound, *i.e.*, Ce6-luminol conjugate (CL), was first synthesized. CL can be efficiently loaded into liposomes, giving rise to a PDT nanotherapy CLL that can be activated in the tumor microenvironment, resulting from the CRET effect of CL under oxidative stress. After demonstrating *in vitro* antitumor effects of CLL, a PDT combination nanotherapy was developed by packaging $^{177}$Lu into CLL. In-depth *in vivo* studies were then conducted to examine therapeutic effects of the engineered PDT liposomes in mice bearing lung tumor xenografts and a mouse model of breast cancer lung metastasis. Antitumor mechanisms of PDT liposomes were also explored by *in vitro* and *in vivo* studies.

## 2. Materials and methods

### 2.1. Materials

1,2-Dihexadecanoyl-rac-glycero-3-phosphocholine (DPPC), dimethylformamide (DMF), *N*,*N*-diisopropylethylamine (DIPEA), dimethyl sulfoxide (DMSO), 2-(7-azabenzotriazol-1-yl)-*N*,*N*,*N*′,*N*′-tetramethyluroniumhexafluorophosphate (HATU), and luminol

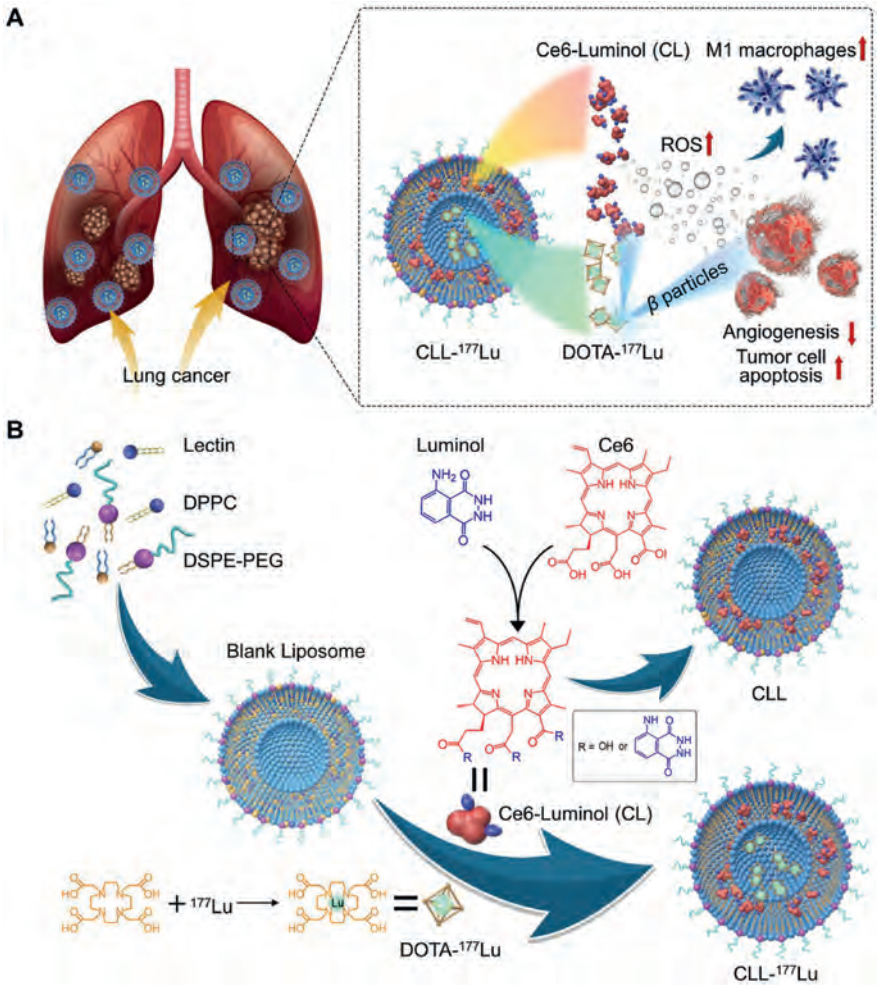


**Scheme 1** Schematic illustration of engineering of dual-functional liposomes for simultaneous *in situ*-triggered photodynamic therapy (PDT) and radiotherapy. (A) A sketch showing the facile development of dual-functional liposomes for the synergistic treatment of cancers by ROS-activatable PDT and $^{177}$Lu-mediated radiotherapy. (B) Chemical structure and synthesis of a ROS-triggerable photosensitizing material, *i.e.*, luminol-conjugated Ce6 (CL), as well as preparation of CL-containing PDT liposomes (CLL) and dual-functional liposomes containing CL and $^{177}$Lu (CLL-$^{177}$Lu).

were purchased from Aladdin Inc. (Shanghai, China). 2′,7′-Dichlorodihydrofluorescein diacetate (DCFH-DA) and cell counting kit-8 (CCK8) were obtained from MedChemExpress (Elizabeth, NJ, USA). Cholesterol (CHOL), 1,4,7,10-tetraazacyclododecane-*N*,*N*′,*N*,*N*′-tetraacetic acid (DOTA), and 2-quinolinol (2-HQ) were provided by Macklin Co., Ltd. (Shanghai, China). Liberase and 4′,6-diamidino-2-phenylindole (DAPI) were obtained from Sigma−Aldrich (Saint Louis, MO, USA). ACK lysis buffer and deoxyribonuclease (DNase I) were purchased from Solarbio Co., Ltd. (Beijing, China). 1,2-Distearoyl-*sn*-glycero-3-phosphoethanolamine-*N*-[methoxy(polyethylene glycol)-2000] (DSPE-PEG) was purchased from Xi'an Ruixi Biological Technology Co., Ltd. (Xi'an, China). Chlorin e6 (Ce6) was obtained from Frontier Scientific Inc. (Newark, NJ, USA). HEPES and terminal deoxynucleotidyl transferase dUTP nick-end labeling (TUNEL) agent and singlet oxygen sensor green reagent were purchased from Beyotime Biotechnology Co., Ltd. (Shanghai, China). Si-DMA agent was purchased from Dojindo Laboratories (Kumamoto-Ken, Japan). G-25 column was purchased from Bersee (Beijing, China). $^{177}$Lu was supplied by the Affiliated Hospital of Southwest Medical University (Luzhou, China). Dulbecco's modified Eagle's medium (DMEM), Roswell Park Memorial Institute (RPMI)-1640 medium, and fetal bovine serum (FBS) were obtained from HyClone Laboratories (Logan, UT, USA). Annexin V-FITC (Annexin V) detection kit was obtained from Elabscience Biotechnology Co., Ltd. (Wuhan, China). iNOS monoclonal antibody-Alexa Fluor 488 was purchased from Thermo Fisher Scientific Inc. (Waltham, MA, USA).

### 2.2. *Synthesis and characterization of luminol-conjugated Ce6 (CL)*

A new *in situ* activatable photosensitizer, *i.e.*, CL, was synthesized by directly conjugating luminol with Ce6. Specifically, 20 mg Ce6 and 57.3 mg HATU were weighed in a stub vial, vacuumed, and nitrogen-ventilated before 8 mL of DMF was added in an ice bath, which was then dissolved, followed by injection of 0.1 mL of DIPEA. After reaction for 0.5 h, 14.2 mg luminol dissolved in 2 mL of DMF was added and allowed for reaction for 24 h. Then the solution was vortexed and concentrated. The reaction solution was extracted three times with ethyl acetate, washed three times with dilute hydrochloric acid (0.5 mol/L), dried with anhydrous magnesium sulfate, filtered, and dried overnight under vacuum. The obtained dark green powder CL was characterized using $^{1}$H NMR (Agilent, 600 MHz DD2, Santa Clara, CA, USA), Fourier transform infrared (FT-IR, PerkinElmer, Spectrum 100, Waltham, MA, USA), and matrix-assisted laser desorption/ionization time-of-flight (MALDI-TOF) mass spectroscopy (Shimadzu, Maldi-7090, Kyoto, Japan).

### 2.3. *Fabrication of CL-containing liposomes*

DPPC, CHOL, CL, and DSPE-PEG were dissolved in a mixture of chloroform and methanol with a volume ratio of 9:1. The weight ratio of DPPC to CHOL was 10:1, and the DPPC/CL weight ratio was 10:1. The total molar content of DSPE-PEG was 5% (mol/mol). Once all these materials were fully dissolved, the solvent was removed by rotary evaporation, resulting in the formation of a uniform film. Hydration was performed by adding 10 mL of deionized water to the film, followed by heating the solution to 40 °C in a rotary evaporator and rotating at a consistent speed for 10 min. Subsequently, the mixture was subjected to sonication in a water bath for 15 min, at a sonication power of 40 W and with an interval of 1 s for 2 min. Then the supernatant was collected to obtain the CL-containing liposomes (CLL).

### 2.4. *Fabrication of CL/$^{177}$Lu-containing liposomes (CLL-$^{177}$Lu) and liposomes containing $^{177}$Lu (L-$^{177}$Lu)*

Preparation of the uniform film was carried out following the same procedures described for CLL. During the hydration step, 2 mL of HEPES buffer containing 2 mg DOTA was added. After heating and spinning, the system was sonicated and centrifuged to obtain DOTA-loaded liposomes. Moreover, un-encapsulated DOTA in the liposome solution was removed using a G-25 desalting column. Subsequently, the liposome solution was incubated with a $^{177}$Lu solution containing 0.314 mmol/L 2-HQ for 1 h at 37 °C. The G-25 desalting column was also used to remove free $^{177}$Lu. Then CL/$^{177}$Lu-loaded liposomes were obtained, which were denoted as CLL-$^{177}$Lu. To optimize the encapsulation efficiency of $^{177}$Lu, $^{177}$Lu-loaded liposomes were prepared using various $^{177}$Lu/DPPC feeding ratios, including 0.5:1, 1:1, and 2:1 (mCi:mg, 1 mCi = 37 MBq). Following the similar procedures, $^{177}$Lu-containing liposomes (L-$^{177}$Lu) were prepared.

### 2.5. *Characterization of different liposomes*

The particle size and $\zeta$-potential values of CLL, L-$^{177}$Lu, and CLL-$^{177}$Lu were measured using a Malvern Zetasizer Nano ZS instrument (Malvern, ZEN3690, Worcs, UK) at 25 °C. Transmission electron microscopy (TEM, Thermo Fisher, TECNAI-10, Waltham, MA, USA) was employed to observe the morphology of different liposomes after staining with 2% phosphotungstic acid. Radioactivity was measured after L-$^{177}$Lu or CLL-$^{177}$Lu was purified to calculate encapsulation efficiency of $^{177}$Lu. Furthermore, the loading content of CL was measured using a UV−Visible spectrophotometer. To determine the colloidal stability of CLL-$^{177}$Lu in different media, CLL-$^{177}$Lu was dispersed in deionized water, PBS (pH 7.4), RPMI-1640 medium, DMEM, and FBS. During varying time periods, variations in the particle size were measured. Furthermore, the fluorescence spectra of CLL and CLL-$^{177}$Lu in water were measured using a fluorescence spectrophotometer (Hitachi, F-7000, Tokyo, Japan), while Ce6 and CL dissolved in DMSO served as controls.

### 2.6. *Evaluation of the CRET effect and ROS-responsive character of CL*

To test the CRET effect, CL at 0.05 mg/mL CL and an equivalent of luminol were added into a black 96-well plate. After the addition of 100 mmol/L $H_2O_2$, luminescence images were captured with or without various emission filters (580, 640, 680, 740, and 780 nm), in the absence of external light (Vilber, Newton 7.0, Paris, France). Furthermore, the ROS-responsive character of CL or CLL at 50 μg/mL was assessed at $H_2O_2$ concentrations varying from 0 to 200 μmol/L, and images were taken with an exposure time of 5 min.

### 2.7. *Cell culture*

Human non-small cell lung cancer A549 cells were cultured in DMEM containing 10% FBS and 1% penicillin/streptomycin at 37 °C and 5% $CO_2$. Mouse breast cancer 4T1 cells and 4T1-GFP cells were cultured in RPMI 1640 supplemented with 10% FBS

and 1% penicillin/streptomycin. L929 mouse fibroblasts and H9C2 rat cardiomyocytes were cultured in DMEM supplemented with 10% FBS and 1% penicillin/streptomycin at 37 °C in a 5% $CO_2$ incubator.

### 2.8. *In vitro cellular uptake of CLL, $^{177}$Lu, and CLL-$^{177}$Lu in 4T1 or A549 cells*

To evaluate cellular uptake of CLL and CLL-$^{177}$Lu in 4T1 cells, $1 \times 10^5$ cells were seeded into 24-well plates and incubated overnight for cell attachment. Then cells were separately incubated with 1 mL of fresh medium containing CLL or CLL-$^{177}$Lu at 50 μg/mL. Following incubation for predetermined durations of time (0, 15, 30, 60, 120, and 240 min), the culture medium was removed, and cells were washed twice with sterile PBS before undergoing trypsinization. The cells were collected by centrifugation at 1000 rpm (Eppendorf, 5804R, Hamburg, Germany) for 5 min and resuspended in 200 μL of pre-cooled PBS. The intracellular fluorescence intensity of CL was measured by flow cytometry (Becton Dickinson, FACSCelesta, Franklin Lakes, NJ, USA).

Moreover, confocal laser scanning microscopy (CLSM, Zeiss, LSM800, Oberkochen, Germany) was utilized to further investigate cellular uptake profiles. To this end, sterile slides were arranged into 24-well plates and exposed to 1 mL of culture medium containing $1 \times 10^5$ 4T1 cells. Following the same experimental procedures as mentioned above, 4T1 cells were treated with paraformaldehyde for 10 min and stained with DAPI for 5 min. After treatment with an anti-fluorescence quenching blocker, fluorescence images were acquired by CLSM (Zeiss). In a separate study, the phagocytic capacity of A549 cells towards CLL or CLL-$^{177}$Lu was also evaluated by flow cytometry (Becton Dickinson) and CLSM (Zeiss) based on the aforementioned experimental protocols.

To compare differences in cellular uptake behaviors among CLL, $^{177}$Lu, and CLL-$^{177}$Lu, $1 \times 10^5$ 4T1 cells or A549 cells were seeded into 24-well plates and incubated overnight to facilitate cell attachment. Subsequently, the cells were separately treated with 1 mL of aqueous solution containing 50 μg/mL CLL, 50 μg/mL CLL-$^{177}$Lu, or 3.3 MBq/mL $^{177}$Lu. The control group was treated with fresh medium alone, and the radioactivity of $^{177}$Lu was equal to that in CLL-$^{177}$Lu. After incubation for 4 h, the culture medium was removed, and cells were rinsed twice with sterile PBS and subjected to trypsinization. Following centrifugation at 1000 rpm (Eppendorf) for 5 min, the cells were resuspended in 200 μL of pre-cooled PBS. The intracellular fluorescence intensity of CL was quantified using flow cytometry (Becton Dickinson), while the radioactivity of $^{177}$Lu in the cells was measured using a γ-counter (USTC Zonkia, GC-911, He Fei, China).

### 2.9. *In vitro antitumor activities of CLL, $^{177}$Lu, and CLL-$^{177}$Lu*

To assess the antitumor activity of CLL, $1 \times 10^4$ 4T1 cells were inoculated in 96-well plates and allowed to fully attach overnight. Different concentrations of CLL (ranging from 0 to 200 μg/mL) were added, while blank liposomes without CL were used as a control. After incubation for 24, 48, or 72 h, the culture medium was removed and replaced with solution containing 10 μL of the CCK8 reagent. Following 2 h of incubation, the absorbance at 450 nm was measured to calculate cell viability. Similar procedures were followed to evaluate antitumor effects of CLL in A549 cells. In parallel, the antitumor activity of CLL and CLL-$^{177}$Lu were further examined in 4T1 or A549 cells, with concentrations ranging from 0 to 1000 μg/mL, to determine the half maximal inhibitory concentration ($IC_{50}$) of CLL and CLL-$^{177}$Lu. Briefly, $1 \times 10^4$ 4T1 cells were incubated in 96-well plates and allowed to adhere overnight, followed by addition of CLL or CLL-$^{177}$Lu. After incubation for 48 h, the absorbance at 450 nm was measured to calculate cell viability (Molecular devices, Emax plus, Sunnyvale, CA, USA).

In a separate study, antitumor effects of CLL, $^{177}$Lu, and CLL-$^{177}$Lu were further compared, using $1 \times 10^4$ 4T1 cells or A549 cells seeded into 96-well plates. After overnight incubation, cells were treated with $^{177}$Lu with the radioactivity ranging from 0 to 13.3 MBq/mL, while the concentrations of CLL and CLL-$^{177}$Lu varied from 0 to 200 μg/mL. The radioactivity levels in CLL-$^{177}$Lu also ranged from 0 to 13.3 MBq/mL. After treatment for 24, 48, and 72 h, cell viability was determined *via* CCK8 assay.

### 2.10. *Cytotoxicity evaluation of CLL and CLL-$^{177}$Lu in non-tumor cells*

To evaluate the cytotoxicity of CLL and CLL-$^{177}$Lu in non-tumor cells, L929 mouse fibroblasts or H9C2 rat cardiomyocytes were seeded in 96-well plates at $1 \times 10^4$ cells per well and cultured for 12 h. Subsequently, various concentrations of CLL or CLL-$^{177}$Lu (ranging from 0 to 1000 μg/mL) were added and incubated for 24 h. Thereafter, the supernatant was removed and replaced with 100 μL of fresh medium containing 10 μL of the CCK-8 reagent. Following 1 h incubation, the absorbance at 450 nm was measured to assess the cell viability of fibroblasts and cardiomyocytes.

### 2.11. *In vitro evaluation of intracellular ROS generation in 4T1 or A549 cells treated with CLL, $^{177}$Lu, or CLL-$^{177}$Lu*

Firstly, the influence of CLL on intracellular ROS generation was investigated. A total of $1 \times 10^5$ 4T1 cells or A549 cells were seeded in each well of 24-well plates. After overnight incubation, cells were exposed to 1 mL of different concentrations of blank liposomes or CLL, varying from 0 to 200 μg/mL. After 24 h of incubation, the cells were washed twice using sterile PBS prior to the addition of a medium containing 10 μmol/L DCFH-DA. Following 20 min of incubation, the supernatant was discarded, and the cells were washed twice using sterile PBS. Then the cells were trypsinized, collected by centrifugation at 1000 rpm (Eppendorf) for 5 min, and resuspended in 200 μL of pre-cooled PBS. The fluorescence intensity of DCFH-DA was measured by flow cytometry (Becton Dickinson).

Further, the ROS-inducing capacity of CLL, $^{177}$Lu, and CLL-$^{177}$Lu were compared in 4T1 cells or A549 cells. Briefly, $1 \times 10^5$ 4T1 or A549 cells were seeded in each well of 24-well plates and incubated overnight. Subsequently, the cells were separately treated with 1 mL of aqueous solution containing 50 μg/mL CLL, 50 μg/mL CLL-$^{177}$Lu, or 3.3 MBq/mL $^{177}$Lu. The control group was treated with fresh medium alone. The radioactivity of $^{177}$Lu was equal to that in CLL-$^{177}$Lu. Following the aforementioned treatment procedures, the fluorescence intensity of DCFH-DA was quantified by flow cytometry (Becton Dickinson). Moreover, confocal images were captured to evaluate the intracellular ROS levels. For this purpose, sterile slides were positioned in 24-well plates, onto which either 4T1 or A549 cells were planted and treated with CLL, CLL-$^{177}$Lu, or $^{177}$Lu. After

staining with DAPI and DCFH-DA, CLSM (Zeiss) observation was performed.

Following similar procedures, the dose-dependent effects of CLL-$^{177}$Lu on intracellular ROS generation were also investigated in 4T1 and A549 cells by flow cytometry (Becton Dickinson) and CLSM (Zeiss). The effects of $^{177}$Lu on intracellular ROS generation were assessed in 4T1 cells by flow cytometry (Becton Dickinson). The cell density was kept at $1 \times 10^5$ cells/well. The radioactivity of $^{177}$Lu was changed from 0.7 to 13.3 MBq/mL, while the concentration of CLL-$^{177}$Lu ranged from 0 to 200 μg/mL (equivalent to the radioactivity of 0−13.3 MBq/mL). After 24 h of incubation, the same treatments were implemented before measurements *via* flow cytometry (Becton Dickinson) and CLSM (Zeiss).

### 2.12. *In vitro evaluation of singlet oxygen ($^1O_2$) generation capacity of CLL*

The $^1O_2$ generation ability of CLL in a cuvette was measured with the singlet oxygen sensor green (SOSG) reagent. Firstly, different doses of CLL (varying from 0 to 50 μg/mL) were mixed with 100 mmol/L $H_2O_2$. Then, 5 μmol/L SOSG was added into each well to initiate the reaction and fluorescence intensity was determined using a spectrofluorometer at excitation/emission wavelengths of 504/535 nm after 0.5 h incubation. Furthermore, the effect of various concentrations of $H_2O_2$ (including 0.01, 0.1, 1, and 10 mmol/L) at a fixed CLL concentration of 50 μg/mL was evaluated using the same method.

In a separate study, confocal images were captured to evaluate the dose-dependent effects of CLL on $^1O_2$ generation in 4T1 and A549 cells. Briefly, sterile slides were positioned in 24-well plates, onto which either 4T1 or A549 cells were planted at a density of $1 \times 10^5$ cells per well and treated with various CLL concentrations (from 0 to 200 μg/mL). After 24 h of incubation, the cells were stained with 75 nmol/L Si-DMA and incubated for another 24 h. Then CLSM (Zeiss) observation was performed.

### 2.13. *In vitro evaluation of apoptosis of 4T1 and A549 cells after treatment with CLL, $^{177}$Lu, or CLL-$^{177}$Lu*

Briefly, $3 \times 10^5$ 4T1 cells were seeded into 6-well plates in each well. The cells were treated with 1 mL of culture medium containing 50 μg/mL CLL, 50 μg/mL CLL-$^{177}$Lu, or 3.3 MBq/mL $^{177}$Lu for 24 h. Cells treated with fresh medium served as the control. Following incubation, the cells were trypsinized, washed twice with PBS, and resuspended in 200 μL of Annexin V binding buffer. Subsequently, Annexin V and DAPI were added and incubated at room temperature for 20 min in the dark, followed by analysis *via* flow cytometry (Becton Dickinson). In addition, $5 \times 10^4$ 4T1 cells were seeded onto sterilized glass coverslips in 12-well plates overnight. The cells were treated with CLL, $^{177}$Lu, or CLL-$^{177}$Lu and incubated for 24 h. After fixation with 4% paraformaldehyde, TUNEL apoptosis analysis was conducted according to the manufacture's protocol. Fluorescence microscopy observation was performed using CLSM (Zeiss). The same protocols were applied to evaluate the effects of CLL, $^{177}$Lu, and CLL-$^{177}$Lu on apoptosis of A549 cells.

### 2.14. *In vitro evaluation of macrophage M1 polarization after treatment with different liposomes*

RAW264.7 macrophages were seeded at a density of $1 \times 10^5$ cells per well in 24-well plates and allowed to incubate overnight. Then cells were treated with 1 mL of 50 μg/mL CLL, 50 μg/mL CLL-$^{177}$Lu, or 3.3 MBq/mL $^{177}$Lu. The control group was treated with fresh medium. After 24 h, the culture medium was removed and the cells were thoroughly washed twice using sterile PBS, trypsinized, and collected *via* centrifugation at 1000 rpm (Eppendorf) for 5 min. Subsequently, the cells were incubated with CD86 and F4/80 antibodies for 30 min, followed by centrifugation and PBS washing before resuspension in 200 μL of prechilled PBS. Finally, the cells were analyzed by flow cytometry (Becton Dickinson). Following the same procedures, the dose-dependent effects of CLL-$^{177}$Lu on macrophage M1 polarization was also examined. In this case, the doses of CLL-$^{177}$Lu ranged from 0, 10, 20, 50, 100, to 200 μg/mL.

In another study, RAW264.7 cells were seeded at a density of $1 \times 10^5$ cells per well in 24-well plates and incubated overnight. Subsequently, the cells were treated with various doses of CLL, $^{177}$Lu, or CLL-$^{177}$Lu. The control group was treated with fresh medium. After 24 h, the culture medium was removed, and the cells were incubated with iNOS antibody for 30 min prior to CLSM (Zeiss) observation.

To explore the mechanism underlying the macrophage phenotype-regulating capability of CLL-$^{177}$Lu, RAW264.7 cells were planted at a density of $1 \times 10^6$ cells per well in 24-well plates and incubated overnight. Then the cells were treated with 200 μg/mL CLL-$^{177}$Lu, while the cells treated with medium alone served as a control. After 24 h of incubation, the cells were collected for RNA-sequencing (RNA-seq) analysis by the standard procedures.

### 2.15. *Animals*

Male and female BALB/c mice (18−20 g, 6−8 weeks old) were obtained from the Army Medical University Animal Center. Male nude mice (18−20 g, 6−8 weeks old) were supplied by Ensiweier Co., Ltd. (Chongqing, China). Animal care and experimental procedures were approved by the Animal Ethical and Experimental Committee of Army Medical University (Third Military Medical University, Chongqing, China).

### 2.16. *Biodistribution and pharmacokinetic profiles of CLL-$^{177}$Lu in tumor-bearing mice*

A549 tumor xenografts were established in nude mice by subcutaneous injection of $1 \times 10^7$ cells into the right axilla[48,49]. When the tumor volume reached 100 mm$^3$, different treatments were performed. To investigate the distribution of CLL-$^{177}$Lu in tumor tissues, 200 μL of 125 μg/mL CLL-$^{177}$Lu was administrated by intravenous (i.v.) injection through the tail vein in mice. Mice treated with the same dose of CL served as the control. At 24 and 48 h after treatment, *in vivo* imaging was carried out after the mice were anaesthetized with isoflurane.

In a separate study, the pharmacokinetic and tissue distribution profiles of CLL-$^{177}$Lu were investigated in mice with 4T1 tumors. Briefly, female BALB/c mice were injected subcutaneously with $2 \times 10^5$ cells into the left abdominal mammary fat pad to establish a 4T1 tumor model. Once the tumor volume reached approximately 80 mm$^3$, the mice received i.v. injection of 200 μL of 625 μg/mL CLL-$^{177}$Lu through the tail vein. Mice treated with saline served as the control. *In vivo* imaging (Vilber) was conducted at various time points (0, 2, 6, 12, 24, 48, and 72 h) after anaesthetizing with isoflurane. Then the mice were euthanized to collect tumors, major organs (including the heart, liver, spleen,

lung, and kidney), and blood samples, which were subjected to *ex vivo* imaging, with an excitation wavelength of 640 nm. To determine the concentrations of CLL-$^{177}$Lu in blood samples, 40 μL of CLL-$^{177}$Lu with concentrations ranging from 0 to 625 μg/mL, was mixed with an equal volume of the blank murine blood in a black 96-well plate. Subsequently, fluorescence intensities were measured and the standard curve was established.

### *2.17. In vivo antitumor effects of CLL-$^{177}$Lu in a mouse model of breast cancer lung metastasis*

A mouse model of breast cancer lung metastasis was established by i.v. injection of $1 \times 10^7$ 4T1-GFP cells *via* the tail vein of BALB/c mice. Treatment was conducted when lung metastases became evident, *i.e.*, approximately 4 weeks after cell injection[50]. After 4 weeks, the model mice were randomly assigned to four groups ($n = 5$). The model group received PBS *via* the tail vein, while the remaining three therapy groups were treated with CLL-$^{177}$Lu at 0.19, 0.37, and 0.74 GBq/kg according to the radioactivity of $^{177}$Lu in CLL-$^{177}$Lu. The same treatment was repeated one week later. At the 5th day subsequent to the second administration, the mice were euthanized, and lung tissues were collected for analysis of 4T1-GFP tumor cells *via* flow cytometry. Furthermore, the ROS levels in the tumor tissues were quantified by both flow cytometry (Becton Dickinson) and fluorescence microscopy (Zeiss). In addition, tumor tissue sections were prepared for histological examination of the iNOS expression levels and cell apoptosis using TUNEL staining.

In a separate study, *in vivo* antitumor efficacies of CLL, $^{177}$Lu, and CLL-$^{177}$Lu were compared in mice with breast cancer lung metastasis. In this case, the model group received PBS, while the other three groups were separately treated with CLL at 5 mg/kg, $^{177}$Lu at 0.37 GBq/kg, and CLL-$^{177}$Lu at 0.37 GBq/kg (equals to CLL at 5 mg/kg). After different treatments, the mice were euthanized and lung tissues were harvested. The counts of 4T1-GFP tumor cells, ROS levels, M1 macrophages, and apoptotic cells in tumor tissues were also analyzed according to the aforementioned procedures. In addition, $CD4^+$ and $CD8^+$ T cells in blood samples were quantified by flow cytometry (Becton Dickinson).

### *2.18. Antitumor efficacy of CLL-$^{177}$Lu in mice with A549 xenograft tumors*

A549 xenograft tumors in mice were established by i.v. injection of $1 \times 10^7$ A549 cells into the right axilla of nude mice. After 10 days, mice were randomly assigned into four groups. Three therapy groups were treated with CLL-$^{177}$Lu at 0.19, 0.37, and 0.74 GBq/kg of $^{177}$Lu by i.v. injection, while mice in the control group were treated with PBS. Mice were administered with CLL-$^{177}$Lu or PBS twice at an interval of 7 days. During the treatment period, the tumor volumes were monitored every three days using calipers. Five days after the second administration, mice were euthanized, and tumor tissues were collected, photographed, and weighed. Apoptotic cells in the tumors were analyzed by flow cytometry. Tumor cryosections were also observation by confocal microscopy after TUNEL staining. Similarly, ROS levels and the proportion of M1 macrophages in tumor tissues were analyzed. In another cohort study, therapeutic effects of $^{177}$Lu, CLL, and CLL-$^{177}$Lu were compared in mice with A549 tumor xenografts. In this case, mice were separately treated with PBS, $^{177}$Lu at 0.37 GBq/kg, CLL at 5 mg/kg, and CLL-$^{177}$Lu at 0.37 GBq/kg (equals to CLL at 5 mg/kg). After different treatments, mice were for different analyses.

### *2.19. Comparison of antitumor effects of CLL-$^{177}$Lu and L-$^{177}$Lu in mice with 4T1 or A549 xenograft tumors*

To compare antitumor efficacy of CLL-$^{177}$Lu, CL, and L-$^{177}$Lu, 4T1 tumors in female BALB/c mice were established by i.v. injection of $2 \times 10^5$ 4T1 cells into the left abdominal mammary fat pad. Once the tumor volume reached approximately 80 mm$^3$, the mice were randomly assigned into six groups, with five mice per group. Tumor-bearing mice were separately administered the following treatments at 7-day intervals over a 33-day period, including PBS, CL at 0.26 mg/kg, CLL at 5 mg/kg (equals to CL at 0.26 mg/kg), $^{177}$Lu at 0.37 GBq/kg, L-$^{177}$Lu at 0.37 GBq/kg, and CLL-$^{177}$Lu at 0.37 GBq/kg (equals to CLL at 5 mg/kg). During the treatment period, tumor volumes were monitored. On Day 7 following the third administration, mice were euthanized, and tumor tissues were harvested, weighed, and imaged. Lung tissues were also examined for tumor metastasis through H&E staining. Apoptosis analysis was performed after TUNEL staining and observation with confocal microscopy. Similarly, ROS levels were assessed by DHE staining. The proportion of M1 macrophages was evaluated by quantifying the iNOS expression levels, while tumor vascularization was analyzed by CD31 staining.

Moreover, antitumor activity of different liposome therapies was evaluated over a 43-day period in mice with A549 xenograft tumors. In this case, tumors were established by i.v. injection of $1 \times 10^7$ A549 cells into the right axilla of nude mice. After 15 days, mice were randomly divided into six groups, and received different treatments at 7-day intervals, including PBS, CL at 0.26 mg/kg, CLL at 5 mg/kg (equals to CL at 0.26 mg/kg), $^{177}$Lu at 0.37 GBq/kg, L-$^{177}$Lu at 0.37 Gbg/kg, and CLL-$^{177}$Lu at 0.37 GBq/kg (equals to CLL at 5 mg/kg). Tumor volumes were measured throughout the treatment period. On the 28th day, mice were euthanized for different analyses following the aforementioned procedures.

### *2.20. In vivo safety evaluation of CLL-$^{177}$Lu*

During *in vivo* anti-tumor treatment, the body weight of all mice was recorded every three days. After treatment, blood samples were collected for quantification of typical hematological parameters, including white blood cells, hemoglobin, and platelets. Serum levels of markers relevant to liver and kidney functions were also detected, such as alanine aminotransferase (ALT), aspartate aminotransferase (AST), blood urea nitrogen (UREA), and creatinine (CREA). Moreover, histological analyses were conducted for tissue sections of the heart, liver, spleen, lung, and kidney following H&E staining.

In addition, normal female BALB/c mice (aged 6−8 weeks, weighing 18−22 g) were randomly assigned to three groups ($n = 5$). The control group received i.v. injection of 200 μL of saline. The CLL-$^{177}$Lu groups were treated with an equivalent volume of CLL-$^{177}$Lu at either a low dose of 1.5 GBq/kg or a high dose of 3.0 GBq/kg. During the experimental period, the body weight of mice in each group was measured every 4 days, and their behaviors were systematically observed. On the 32nd day post-injection, all mice were euthanized, and blood samples were collected for liver/kidney function analyses. Additionally, major organs were excised, weighed, and subjected to H&E staining for histological analysis.

### 2.21. Statistical analysis

All quantitative data are presented as means ± standard deviation (SD). Statistical analysis was conducted with the software of SPSS23 (IBM, USA) using a one-way ANOVA test with multiple comparisons for experiments containing more than two groups. One-way ANOVA with a two-tailed, unpaired *t*-test was performed for two-group experiments. $P < 0.05$ is considered statistically significant.

## 3. Results and discussion

### 3.1. Engineering and physicochemical characterization of in situ pathologically activatable PDT liposomes based on a ROS-triggerable photosensitizer

An *in situ* ROS-activatable photosensitizer, *i.e.*, CL, was synthesized by conjugating luminol with Ce6 (Scheme 1). Measurement by FT-IR, $^1$H NMR, and MALDI-TOF mass spectrometry revealed successful conjugation of luminol on Ce6 (Supporting Information Fig. S1A−S1C). Specifically, FT-IR spectroscopy revealed appearance of a carbonyl stretching vibration peak ranging from 1715 to 1828 $cm^{-1}$, suggesting the formation of a new amide bond resulting from covalent linking between the carboxyl group of Ce6 and the amino group of luminol. The $^1$H NMR spectrum indicated characteristic proton peaks at 8.1−8.4 ppm corresponding to hydrogen atoms in double bonds of Ce6, while the proton signals at 7.5−8.0 ppm suggested the presence of the benzene ring in luminol. Calculation based on the $^1$H NMR spectrum indicated that approximately two luminol units were conjugated onto each Ce6. Furthermore, MALDI-TOF mass spectrometry affirmed the conjugation of 1−2 luminol units per Ce6 molecule. Fluorescence spectroscopy showed that CL displayed fluorescence properties similar to Ce6, with maximal emission at 675 nm upon excitation at 407 nm (Fig. S1D).

In the presence of $H_2O_2$, both luminol and CL showed notable luminescence signals when no emission filters were applied (Supporting Information Fig. S2A and S2B). By contrast, when filters with different emission wavelengths were used, no luminescence was detected for luminol, while CL displayed notable luminescence at 680 and 740 nm. This result suggested that the luminol group in CL can be activated by ROS, which facilitates the transfer of excited-state energy to the Ce6 unit, thereby resulting in long-wavelength luminescence. Consequently, CL demonstrated a significant CRET effect. Furthermore, luminescence imaging and quantitative analysis revealed that CL exhibited CRET effects even under low ROS conditions (Fig. S2C).

To engineer *in situ* activatable PDT liposomes, CL-loaded liposomes (defined as CLL) were prepared through thin-film hydration, using DPPC, cholesterol, CL, and DSPE−PEG. Of note, the DPPC/CL weight ratio was kept at 10:1. TEM observation suggested that CLL displayed a spherical shape (Fig. 1A). Dynamic light scattering (DLS) measurement indicated that CLL exhibited a relatively narrow size distribution profile (Fig. 1B), with a polydispersity index of 0.16 ± 0.01 and a mean diameter of 129 ± 1 nm. The ζ-potential value of CLL in deionized water was found to be −11.9 ± 0.3 mV (Fig. 1C). Fluorescence quantification indicated that the encapsulation efficiency of CL was 52.0% in CLL. Similar to CL, CLL demonstrated ROS-responsive luminescence properties even at a $H_2O_2$ concentration of 10 μmol/L, indicating the activation of the CRET effect under low ROS conditions (Fig. S2D).

### 3.2. CLL-mediated intracellular ROS generation in tumor cells and in vitro cytotoxic effects of CLL

External light-mediated generation of highly cytotoxic $^1O_2$ by photosensitizers is a prerequisite for PDT[51]. ROS generation capacity is a critical parameter to evaluate the effectiveness of photosensitizing molecules or nanoparticles[52,53]. Hence, the ROS-generation ability of CLL was first assessed in 4T1 and A549 tumor cells. Taking advantage of CL fluorescence, flow cytometry analysis revealed rapid and time-dependent cellular uptake of CLL by 4T1 and A549 tumor cells (Supporting Information Fig. S3).

Then we examined CLL-mediated ROS-generation in 4T1 cells by flow cytometric quantification after staining with DCFH-DA, a broadly used fluorescence probe for ROS[54]. Whereas incubation with various concentrations of blank liposomes without CL did not change the relative ROS levels in 4T1 cells (Fig. 1D), treatment with CLL notably increased the intracellular ROS levels in 4T1 cells, in a clearly dose-dependent manner (Fig. 1E). In A549 cells, we also found CLL-mediated intracellular ROS generation in a dose−response pattern, while blank liposomes showed negligible effects (Fig. 1F and G). Further evaluation using the fluorescence probe SOSG demonstrated that CLL generated $^1O_2$ in a manner dependent on both the $H_2O_2$ concentration and CLL dosage (Supporting Information Fig. S4). In addition, fluorescence observation and quantitative analysis indicated that CLL induced intracellular $^1O_2$ generation in a dose-dependent pattern in both 4T1 and A549 cells, as evidenced by the gradually increased fluorescence intensities of SOSG (Fig. 1H−K).

In line with these results, incubation with various doses of blank liposomes showed no significant effects on the cell viability of 4T1 cells, even after 72 h of incubation (Fig. 1L). By contrast, treatment with CLL significantly reduced cell viability of 4T1 cells, in both time and dose−response profiles. Likewise, CLL notably induced A549 cell death, depending on incubation time and doses (Fig. 1M). After 24 h of incubation, the $IC_{50}$ value of CLL was determined to be 367.5 μg/mL in 4T1 cells and 483.8 μg/mL in A549 cells (Supporting Information Fig. S5), corresponding to a CL dose of 19.1 μg/mL in 4T1 cells and 25.2 μg/mL in A549 cells, respectively. Collectively, these results demonstrated that CLL exhibited anti-tumor effects in both 4T1 and A549 cells, mainly by inducing intracellular ROS/$^1O_2$ generation.

### 3.3. Development of dual-functional liposomes containing CL and a therapeutic radionuclide $^{177}$Lu for combination antitumor therapy

Based on the antitumor activity of the CL-containing liposome CLL, we hypothesize that synergistic effects can be achieved by combining with other anti-tumor agents. As a proof of concept, $^{177}$Lu, one of the most important therapeutic radionuclides in nuclear medicine, was employed to develop CLL-based combination therapy. The dual-functional liposomal combination therapy, termed as CLL-$^{177}$Lu, was prepared following the previously established procedure for CLL. Nevertheless, DOTA was first incorporated in CLL during the film-hydration step to enhance the loading efficiency of $^{177}$Lu. DOTA has been extensively used as a high effective carrier for imaging contrast agents and metal-based radiopharmaceutics[55]. CLL-$^{177}$Lu was then obtained by incubation of DOTA-containing CLL with $^{177}$Lu solution (Fig. 2A). At various formulations based on the $^{177}$Lu/DPPC ratios (mCi/mg) varying from 0.5:1, 1:1, to 2:1, the loading efficiency $^{177}$Lu was higher than 90% (Fig. 2B). Of note, the formulation with the

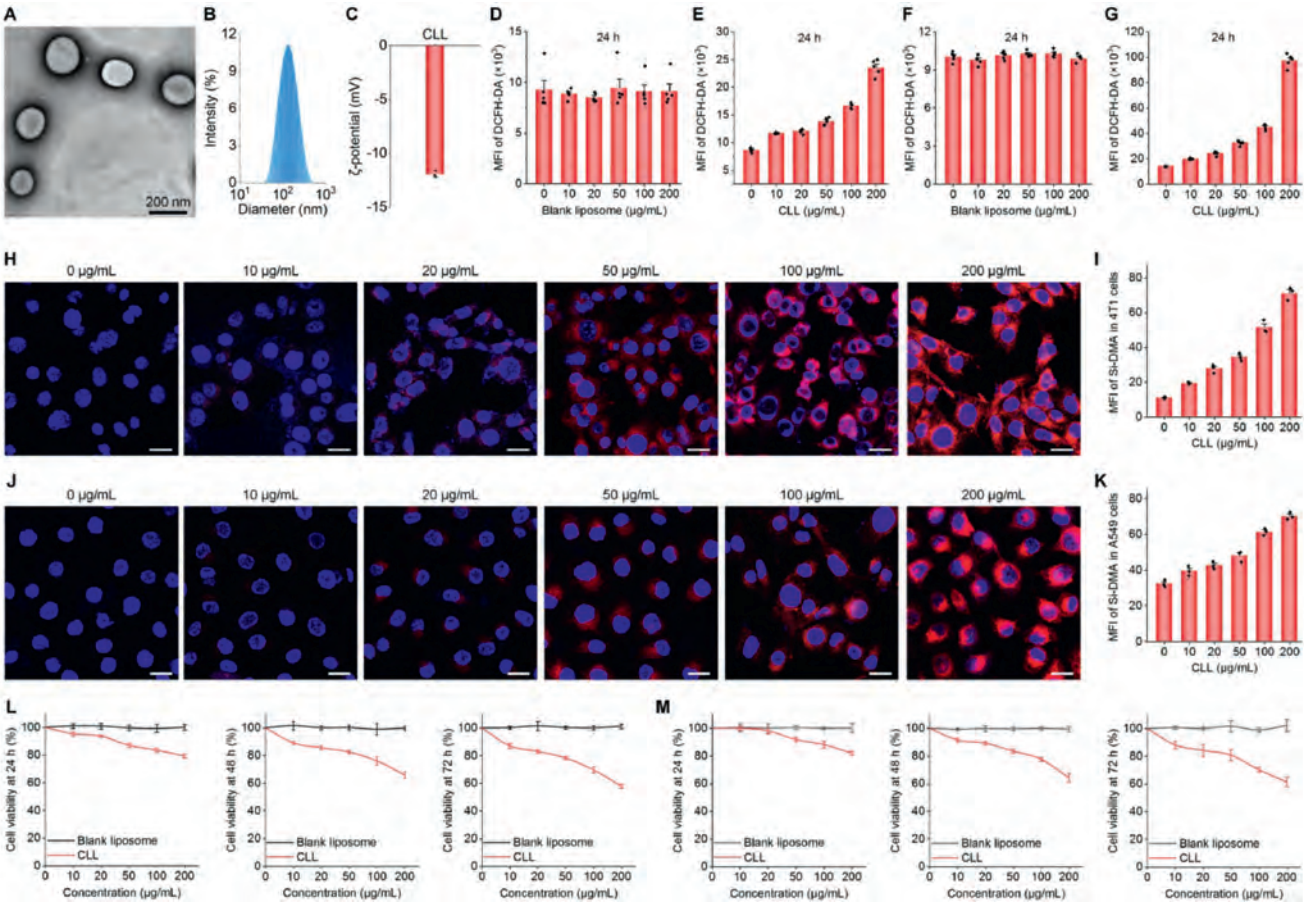


**Figure 1** Physicochemical characterization and *in vitro* antitumor effects evaluations of CLL. (A−C) The TEM image (A), particle size (B), and ζ-potential (C) of CLL. (D−G) Flow cytometric analysis showing mean fluorescence intensity (MFI) in 4T1 cells (D, E) or A549 cells (F, G) after treatment with different doses of blank liposomes (D, F) or CLL (E, G). (H−K) Confocal microscopy images (H, J) and quantitative analysis of MFI (I, K) showing relative $^1O_2$ levels in 4T1 cells (H, I) or A549 cells (J, K) following treatment with various doses of CLL. (L−M) The cell viability values of 4T1 tumor cells (L) or A549 cells (M) following incubation with control liposomes or CLL at various doses for 24, 48, and 72 h. Data are presented as means ± SD (C, I, K, $n = 3$; D−G, L−M, $n = 5$). Scale bars, 20 μm.

$^{177}$Lu/DPPC ratio of 2:1 was used to prepare CLL-$^{177}$Lu for subsequent experiments, due to the high content of $^{177}$Lu.

For the finally obtained liposomal therapy CLL-$^{177}$Lu, TEM observation indicated a spherical shape (Fig. 2C), with the average diameter of 142 ± 2 nm and ζ-potential value of −8.6 ± 0.3 mV (Fig. 2D and E). After incubation in deionized water, PBS, FBS, DMEM, and RMPI1640 for 3 days, no significant change in the average diameter was observed for CLL-$^{177}$Lu (Fig. 2F and Supporting Information Fig. S6), indicating its good colloidal stability. These results suggest that $^{177}$Lu can be efficiently loaded into the ROS-triggerable PDT liposome CLL by the DOTA-based chelating strategy, thus affording a combination antitumor therapy CLL-$^{177}$Lu. Furthermore, both CLL and CLL-$^{177}$Lu exhibited fluorescence emissions characteristic of Ce6 and CL at wavelengths above 650 nm (Supporting Information Fig. S7), endowing them with enhanced capabilities for fluorescence imaging.

### *3.4. CLL-$^{177}$Lu-induced intracellular ROS generation and in vitro antitumor effects*

Then *in vitro* biological effects of CLL-$^{177}$Lu were evaluated. Similar to CLL, both confocal microscopy observation and flow cytometry quantification revealed time-dependent endocytosis of CLL-$^{177}$Lu in 4T1 cells (Fig. 2G−I). After 4 h of incubation, considerably low radioactivity was found in 4T1 cells treated with $^{177}$Lu (Fig. 2J). By contrast, CLL-$^{177}$Lu-treated 4T1 cells showed dramatically higher radioactive counts. Further quantification of intracellular Ce6 fluorescence revealed comparable fluorescence intensities in 4T1 cells post incubation with CLL or CLL-$^{177}$Lu for 4 h (Fig. 2K). These results suggested that packaging into CLL can notably improve intracellular internalization of $^{177}$Lu by 4T1 tumor cells, while incorporation of $^{177}$Lu does not affect cellular uptake performance of CLL.

Subsequently, we examined *in vitro* antitumor activity of CLL-$^{177}$Lu, using $^{177}$Lu and CLL as controls. After 4T1 cells were treated with different formulations, cell viability was gradually reduced, depending on the dosages of liposomes and/or $^{177}$Lu (Fig. 2L). In particular, the reduction in the cell viability of 4T1 cells was closely related to the incubation time. At all three examined time points of 24, 48, and 72 h, the most potent antitumor effect was found for CLL-$^{177}$Lu. Consistently, the highest cell apoptosis was detected for 4T1 cells treated with CLL-$^{177}$Lu for 24 h, compared to the $^{177}$Lu and CLL groups, as implicated by flow cytometry and confocal microscopy analyses (Fig. 2M−P). Further analyses revealed the highest ROS generation in CLL-$^{177}$Lu-treated 4T1 cells (Fig. 2Q and R). Whereas $^{177}$Lu at

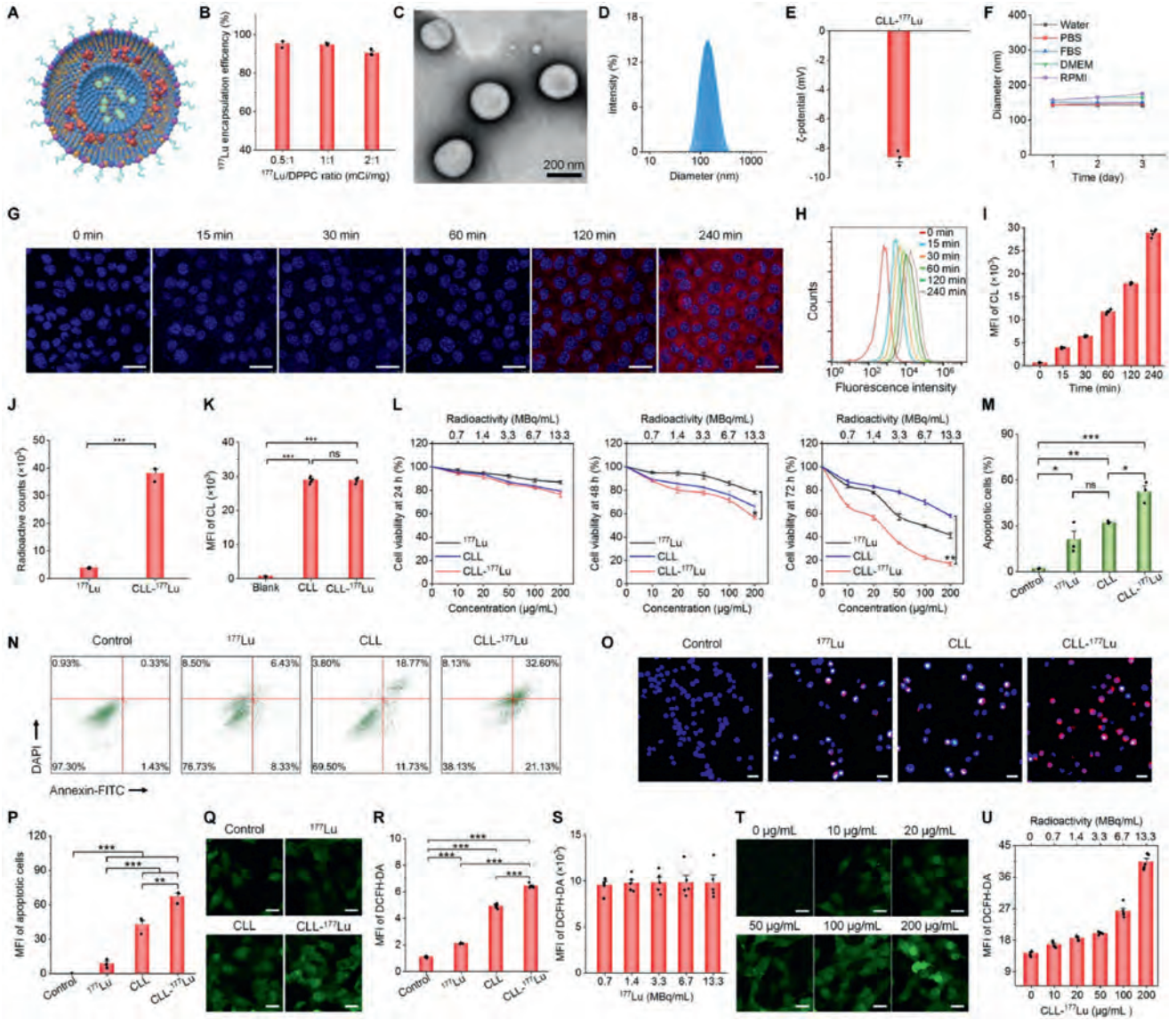


**Figure 2** Engineering, characterization, and *in vitro* anti-tumor evaluations of CLL-$^{177}$Lu. (A) A sketch showing the structure and composition of the dual-functional liposome CLL-$^{177}$Lu. (B) The effect of the $^{177}$Lu/DPPC feeding ratio (mCi/mg, 1 mCi = 37 MBq) on the encapsulation efficiency of $^{177}$Lu in resulting dual-functional liposomes. (C−E) The typical TEM image (C), particle size (D), and ζ-potential (E) of CLL-$^{177}$Lu prepared with the $^{177}$Lu/DPPC ratio of 2:1. (F) Changes in the mean diameter of CLL-$^{177}$Lu in different media during 3 days of incubation. (G) CLSM images show time-dependent cellular internalization of CLL-$^{177}$Lu in 4T1 cells. Scale bars, 20 μm. (H, I) Flow cytometric profiles (H) and quantitative analysis (I) indicate time-dependent phagocytosis of CLL-$^{177}$Lu in 4T1 tumor cells. (J) Comparison of intracellular radioactive counts in 4T1 cells after 4 h of incubation with $^{177}$Lu and CLL-$^{177}$Lu at 3.3 MBq/mL of $^{177}$Lu. (K) Comparison of intracellular fluorescence intensities in 4T1 cells after 4 h of incubation with CLL and CLL-$^{177}$Lu at the same dose. (L) Cell viability of 4T1 tumor cells after incubation with various doses of $^{177}$Lu, CLL, and CLL-$^{177}$Lu for 24, 48, and 72 h. (M−O) Flow cytometric analysis (M, N) and confocal microscopy observation (O, P) indicate apoptosis of 4T1 cells after incubation with $^{177}$Lu (3.3 MBq/mL), CLL (50 μg/mL, equivalent to 2.6 μg/mL CL), or CLL-$^{177}$Lu (containing 50 μg/mL CLL and 3.3 MBq/mL $^{177}$Lu). Scale bars, 10 μm. (Q, R) CLSM images (Q) and quantification (R) showing relative ROS levels in 4T1 cells after treatment with $^{177}$Lu, CLL, or CLL-$^{177}$Lu. Scale bars, 20 μm. (S) Flow cytometric analysis showing the effect of the $^{177}$Lu dosage on relative intracellular ROS levels in 4T1 cells. (T, U) CLSM images (T) and quantitative analysis (U) indicate intracellular ROS generation in 4T1 cells in a CLL-$^{177}$Lu dose-dependent manner. Scale bars, 20 μm. Data are presented as means ± SD (B, E, F, J, M, P, $n$ = 3; I, K, L, R, S, U, $n$ = 5). *$P$ < 0.05, **$P$ < 0.01, ***$P$ < 0.001; ns, not significant.

3.3 MBq/mL also induced a significant increase in ROS production, its effect was remarkably lower than that of CLL at 50 μg/mL. Nevertheless, no significant dose-dependent effects on ROS generation were found for $^{177}$Lu (Fig. 2S). This agrees with the fact that $^{177}$Lu exerts its antitumor effects mainly by emitting $\beta$-particles and internal conversion electrons *via* $\beta$-decay, thus breaking DNA chains of tumor cells, either directly or indirectly[56,57]. For CLL-$^{177}$Lu, its effect on intracellular ROS generation was also dependent on the treatment dosage (Fig. 2T and U). In A549 cells, CLL-$^{177}$Lu also displayed a time-dependent cellular

uptake profile (Fig. 3A–C). Likewise, CLL remarkably increased intracellular internalization of $^{177}$Lu in A549 cells, while comparable cellular uptake was found for CLL-$^{177}$Lu and CLL (Fig. 3D and E). Similarly, both time- and dose-dependent cytotoxicity profiles were observed for CLL-$^{177}$Lu in A549 cells (Fig. 3F), with stronger antitumor activity relative to $^{177}$Lu and CLL, particularly at 48 and 72 h. Apoptosis analysis further indicated the best antitumor effect of CLL-$^{177}$Lu in A549 cells (Fig. 3G–J). Correspondingly, the ROS-inducing capability of CLL-$^{177}$Lu was also stronger than that of $^{177}$Lu and CLL (Fig. 3K and L). Likewise, CLL-$^{177}$Lu induced intracellular ROS generation in A549 cells in a dose–response profile (Fig. 3M and N).

Of note, at 24 h after incubation, CLL-$^{177}$Lu exhibited only slightly increased cytotoxicity in both 4T1 and A549 tumor cells, compared with the same doses of CLL. However, after 48 or 72 h of incubation, CLL-$^{177}$Lu displayed significantly stronger antitumor effects than CLL in these two cell lines. Additionally, at the tested doses, CLL showed markedly higher cytotoxicity at 24 and 48 h, compared to $^{177}$Lu. By contrast, $^{177}$Lu more significantly reduced the cell viability of 4T1 and A549 cells after 72 h of incubation, in comparison to CLL. These results suggest that PDT mainly drives antitumor efficacy at an early stage, while radiotherapy becomes the dominant effect at later stages. In addition, the cytotoxicity data at 72 h were analyzed to calculate the combination index (CI). The results indicated that for both 4T1 and A549 cells, the CI values were less than 1 at CLL-$^{177}$Lu concentrations ranging from 10 to 200 μg/mL, demonstrating a significant synergistic antitumor effect of CLL-$^{177}$Lu, particularly at 50 μg/mL (Fig. S8). Moreover, after 72 h of incubation with 4T1 cells, the $IC_{50}$ value of CLL-$^{177}$Lu was determined to be 56.0 μg/mL, equivalent to 2.9 μg/mL CL and 3.7 MBq/mL $^{177}$Lu (Supporting Information Fig. S9). In A549 cells, the $IC_{50}$ value was 175.3 μg/mL CLL-$^{177}$Lu, which corresponds to 9.1 μg/mL CL and 11.6 MBq/mL $^{177}$Lu. Importantly, cytotoxicity tests in L929 fibroblasts and H9C2 cardiomyocytes showed that cell viability remained above 90% at doses lower than 400 μg/mL (Supporting Information Fig. S10), indicating that CLL-$^{177}$Lu has

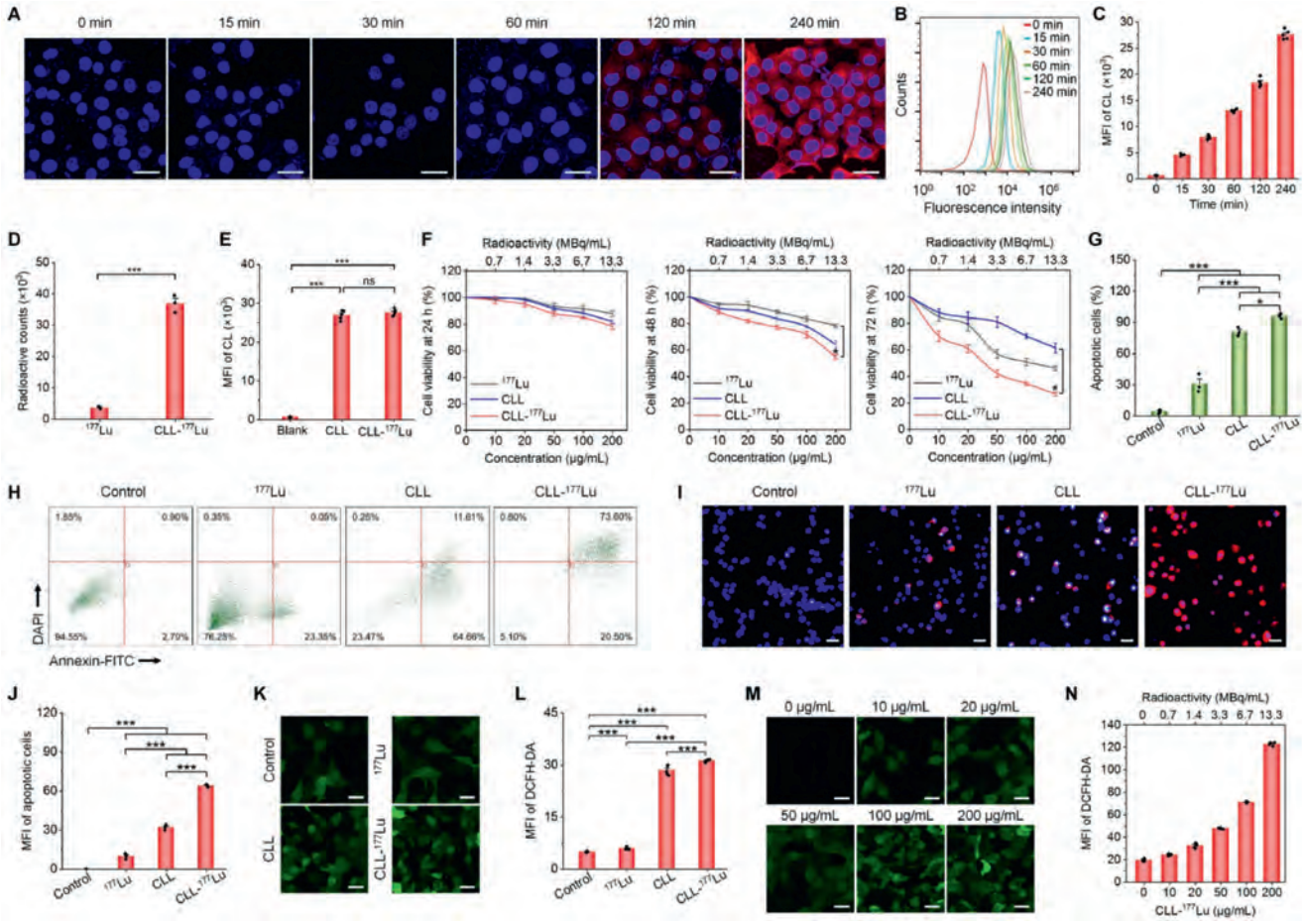


**Figure 3** *In vitro* antitumor effects of CLL-$^{177}$Lu in A549 cells. (A) Confocal microscopy observation of time-dependent cellular internalization of CLL-$^{177}$Lu in A549 cells. Scale bars, 20 μm. (B, C) Flow cytometric profiles (B) and quantification (C) indicate time-dependent endocytosis of CLL-$^{177}$Lu in A549 cells. (D) Comparison of radioactive counts in A549 cells after 4 h of incubation with $^{177}$Lu and CLL-$^{177}$Lu at 3.3 MBq/mL of $^{177}$Lu. (E) Intracellular MFI values in A549 cells after 4 h of incubation with the same dose of CLL and CLL-$^{177}$Lu. (F) Cell viability of A549 cells after incubation with various doses of $^{177}$Lu, CLL, and CLL-$^{177}$Lu for 24, 48, and 72 h. (G–J) Flow cytometry (G, H) and fluorescence microscopy (I, J) analyses of apoptosis of A549 cells after 24 h of incubation with $^{177}$Lu (3.3 MBq/mL), CLL (50 μg/mL, equivalent to 2.6 μg/mL CL), or CLL-$^{177}$Lu (containing 50 μg/mL CLL and 3.3 MBq/mL $^{177}$Lu). Scale bars, 10 μm. (K, L) CLSM images (K) and quantification (L) show relative ROS levels in A549 cells after treatment with $^{177}$Lu, CLL, or CLL-$^{177}$Lu. (M, N) The effect of the CLL-$^{177}$Lu dose on intracellular ROS generation in A549 cells. Scale bars, 20 μm. Data are presented as means ± SD (D, G, J, $n = 3$; C, E, F, L, N, $n = 5$). $^{*}P < 0.05$, $^{***}P < 0.001$; ns, not significant.

low cytotoxic effects on non-tumor cells. Taken together, by loading a radiopharmaceutical $^{177}$Lu into the ROS-activatable PDT liposome CLL, a combination liposome therapy was successfully developed, which demonstrated significantly improved antitumor activity in both 4T1 and A549 tumor cells by simultaneously achieving PDT and radiotherapy.

### 3.5. Therapeutic effects of CLL-$^{177}$Lu in a lung metastasis model

On the basis of desirable *in vitro* cytotoxic effects of CLL-$^{177}$Lu on tumor cells, we first explored its antitumor efficacy in a mouse model of lung cancer. The breast cancer lung metastasis model was established by i.v. injection of 4T1 tumor cells in mice. Since our previous study indicated the presence of pulmonary metastases at week 4 after i.v. injection of 4T1 cells[50], treatment with CLL-$^{177}$Lu at different doses was conducted 4 weeks post cell injection (Supporting Information Fig. S11A). On Day 5 after the final treatment, mice were euthanized and lung tissues were excised for different analyses. Examination of H&E-stained lung sections revealed the presence of multiple metastatic pulmonary nodules and considerable inflammatory cell infiltration in saline-treated model mice (Fig. S11B). Treatment with CLL-$^{177}$Lu, in particular at 0.37 and 0.74 GBq/kg of $^{177}$Lu, considerably inhibited the nodule formation. Correspondingly, TUNEL staining of lung tissues revealed notable cell apoptosis after therapy with CLL-$^{177}$Lu, showing an evidently dose-dependent effect (Fig. S11C). Further flow cytometric analysis of lung tissues indicated that the proportion of 4T1-GFP tumor cells was significantly reduced after intervention with CLL-$^{177}$Lu (Fig. S11D). In line with these findings, we detected significantly increased ROS levels in lung tissues post treatment with CLL-$^{177}$Lu (Fig. S11E). These results demonstrated that the dual-functional combination liposomal therapy CLL-$^{177}$Lu at 0.74 GBq/kg of $^{177}$Lu can effectively inhibit tumor progression in a mouse model of lung cancers mainly by inducing tumor cell apoptosis.

Further, we compared *in vivo* antitumor activity of CLL-$^{177}$Lu (at 0.37 GBq/kg) with the same dose of CLL and $^{177}$Lu, following the above-mentioned treatment procedures (Fig. 4A). After different treatments, inspection of H&E-stained lung tissue sections indicated that all three formulations can effectively inhibit tumor development, resulting in a notable reduction in pulmonary nodules and decreased tumor cell infiltration (Fig. 4B). Consistently, TUNEL staining of lung tissue sections revealed significantly increased cell apoptosis (Fig. 4C), while flow cytometric quantification indicated significantly reduced 4T1-GFP tumor cells (Fig. 4D), following therapy with CLL, $^{177}$Lu, and CLL-$^{177}$Lu. Agreeing with evident antitumor effects, the relative ROS levels in lung tissues were notably increased after treatment with three formulations (Fig. 4E). Moreover, quantitative analysis of $CD4^+$ and $CD^{8+}$ T cell populations in blood samples revealed the most pronounced recruitment and activation effects of CLL-$^{177}$Lu on immune cells (Supporting Information Fig. S12). However, no significant differences were found in the percentages of $CD4^+$ and $CD^{8+}$ T cells between the CLL and $^{177}$Lu groups. Collectively, these results substantiated that CLL itself can notably suppress the development of 4T1 breast cancer lung metastasis in mice, in accordance with its ROS/$^1O_2$-generating capability in 4T1 cells. By combining CLL with the radiotherapy $^{177}$Lu, the obtained dual-functional liposome CLL-$^{177}$Lu exhibited much more superior synergistic antitumor effects in mice.

### 3.6. CLL-$^{177}$Lu induces M1 macrophage polarization to synergize PDT and radiotherapy

The above *in vitro* and *in vivo* results demonstrated that both CLL and CLL-$^{177}$Lu can induce intracellular ROS/$^1O_2$ generation in tumor cells and tumor tissues. Moreover, previous studies substantiated that high levels of ROS can mediate M1 polarization of tumor-associated macrophages, thus potentiating or synergizing tumor immunotherapy[58]. Consequently, we further examined whether CLL-$^{177}$Lu induces M1 polarization of macrophages. After incubation of RAW264.7 macrophages with various doses of CLL-$^{177}$Lu for 24 h, flow cytometry analysis revealed a significantly increased proportion of M1 macrophages (Fig. 5A and B). Even treatment with 10 μg/mL CLL-$^{177}$Lu (containing 0.7 MBq/mL $^{177}$Lu) significantly polarized macrophages to the M1 phenotype. In line with this *in vitro* result, immunofluorescence analysis of tissue sections also showed notably increased M1 macrophages in the lungs from mice with 4T1 cancer lung metastasis, after treatment with different doses of CLL-$^{177}$Lu (Fig. 5C and D). In particular, CLL-$^{177}$Lu at 0.19 Gpq/kg induced a significant increase in the M1 macrophage subpopulation. In addition, we found that $^{177}$Lu and CLL enabled M1 polarization of macrophages after *in vitro* incubation (Fig. 5E and F). Nevertheless, CLL-$^{177}$Lu much more effectively induced polarization, compared to the same dose of $^{177}$Lu and CLL. Similar results were obtained in tissue sections of lungs with 4T1 tumors (Fig. 5G and H).

Moreover, immunofluorescence staining of macrophages treated with CL, $^{177}$Lu, or CLL-$^{177}$Lu revealed a dose-dependent effect on their polarization (Fig. 6A and B). Calculation of the CI further demonstrated that CLL-$^{177}$Lu exhibited a clear synergistic effect in promoting M1 polarization of macrophages at concentrations higher than 10 μg/mL (Fig. 6C). Further, RNA-seq analysis was conducted in RAW264.7 macrophages after treatment with either medium or CLL-$^{177}$Lu to elucidate the underlying mechanisms. The heatmap illustrates the differentially expressed genes (DEGs) between the control and CLL-$^{177}$Lu group (Fig. 6D). A total of 1295 DEGs were identified, including 813 upregulated genes and 482 downregulated genes (Fig. 6E). KEGG enrichment analysis revealed the activation of various biological and metabolic pathways (Fig. 6F), encompassing the NOD-like receptor signaling pathway and pathways associated with ROS. Previous studies have demonstrated that ROS facilitate the M1 polarization of macrophages by activating the MAPK and NF-$\kappa$B signaling pathways, which involve NOD-like receptors and changes in mitochondrial membrane potential[59,60] Consequently, gene set enrichment analysis (GSEA) was performed, and the enrichment plots indicated activated pathways related to NOD-like receptor signaling and ROS (Fig. 6G and H). These findings support the notion that treatment with CLL-$^{177}$Lu can regulate the NOD-like receptor signaling pathway, subsequently activating the MAPK and NF-$\kappa$B signaling pathways, ultimately leading to the polarization of macrophages towards the M1 phenotype. Collectively, in combination with $^{177}$Lu, the obtained dual-functional liposome CLL-$^{177}$Lu exhibited much more potent activity in inducing macrophage polarization, thus synergizing PDT and radiotherapy.

### 3.7. In vivo pharmacokinetic and tissue distribution profiles of CLL-$^{177}$Lu in mice with tumor xenografts

Before therapeutic evaluations in mice with subcutaneous tumor xenografts, we first assessed the tumor-targeting capability of

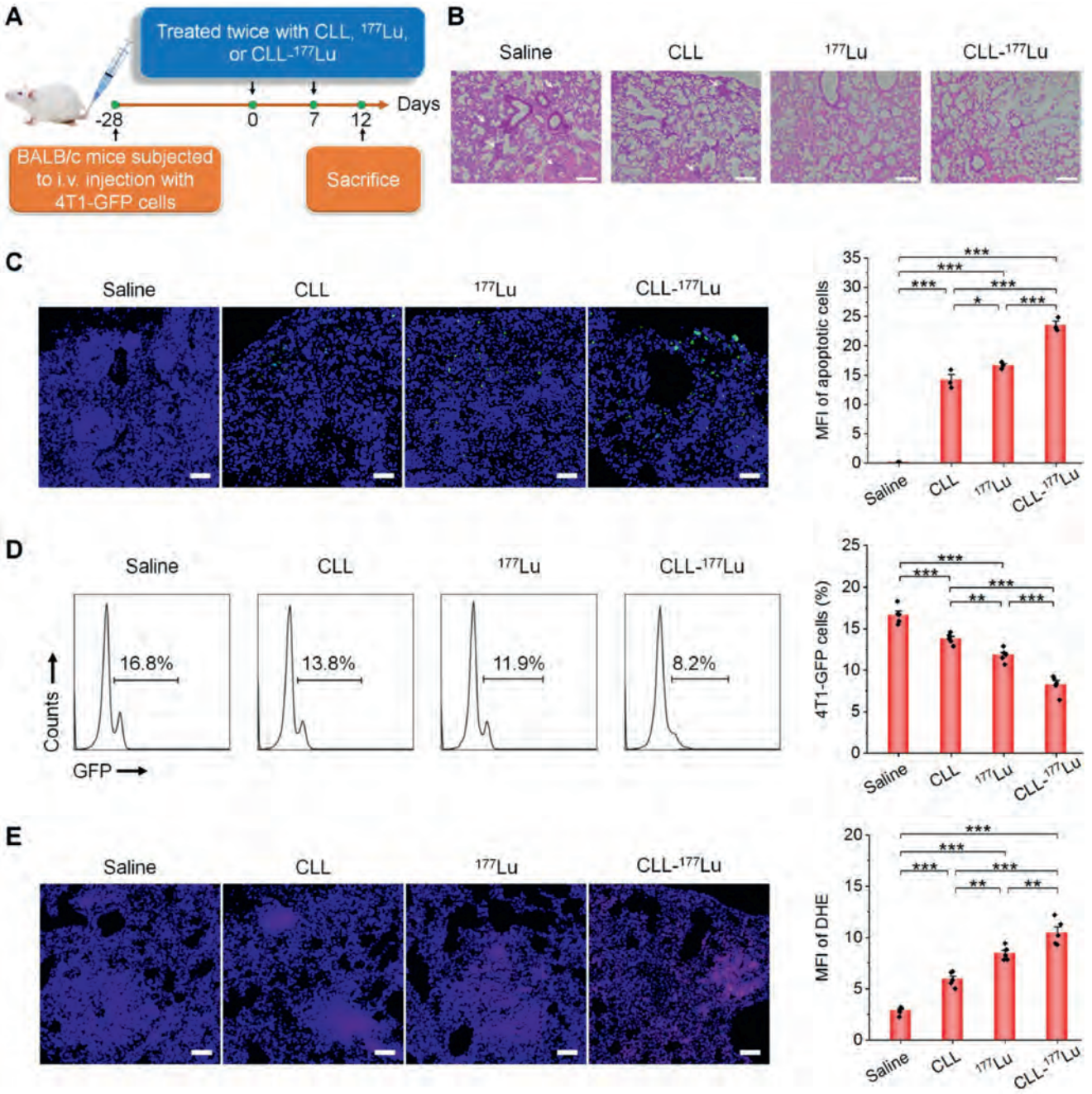


**Figure 4** Comparison of *in vivo* antitumor effects of $^{177}$Lu, CLL, and CLL-$^{177}$Lu in a mouse model of breast cancer lung metastasis. (A) A sketch shows treatment regimens. (B) Microscopic images of H&E-stained lung sections after different treatments. Scale bars, 50 μm. White arrows indicate metastatic pulmonary nodules. (C) CLSM images (left) and quantitative analysis (right) showing cell apoptosis in the lungs. (D) Flow cytometric profiles (left) and quantitative analysis (right) of 4T1-GFP tumor cells in lungs. (E) CLSM images (left) and quantification (right) indicating relative ROS levels in the DHE-stained lungs. Scale bars, 20 μm. Data are presented as means ± SD (C, $n = 3$; D, E, $n = 5$). $^{*}P < 0.05$, $^{**}P < 0.01$, $^{***}P < 0.001$.

CLL-$^{177}$Lu. To this end, A549 cells were inoculated into the right axilla of nude mice by subcutaneous injection. On Day 10 after cell inoculation, we found that CLL-$^{177}$Lu delivered *via* i.v. injection exhibited notable accumulation in A549 lung tumors at 24 and 48 h post administration (Supporting Information Fig. S13). Additionally, we investigated pharmacokinetic and tissue distribution profiles of CLL-$^{177}$Lu in mice with 4T1 xenograft tumors. After i.v. injection of CLL-$^{177}$Lu, fluorescence imaging of blood samples indicated that CLL-$^{177}$Lu remained in the bloodstream for nearly 48 h (Supporting Information Fig. S14A). Using an established calibration curve, the blood concentrations of CLL-$^{177}$Lu were calculated and plotted against time (Fig. S14B). Analysis of the fluorescence intensity−time curve validated that CLL-$^{177}$Lu may circulate in the blood for at least 24 h, with a half-life of 18.2 h and an area under the curve ($AUC_{0-t}$) of 1591.7 mg/L•h. Also, *ex vivo* fluorescence imaging revealed

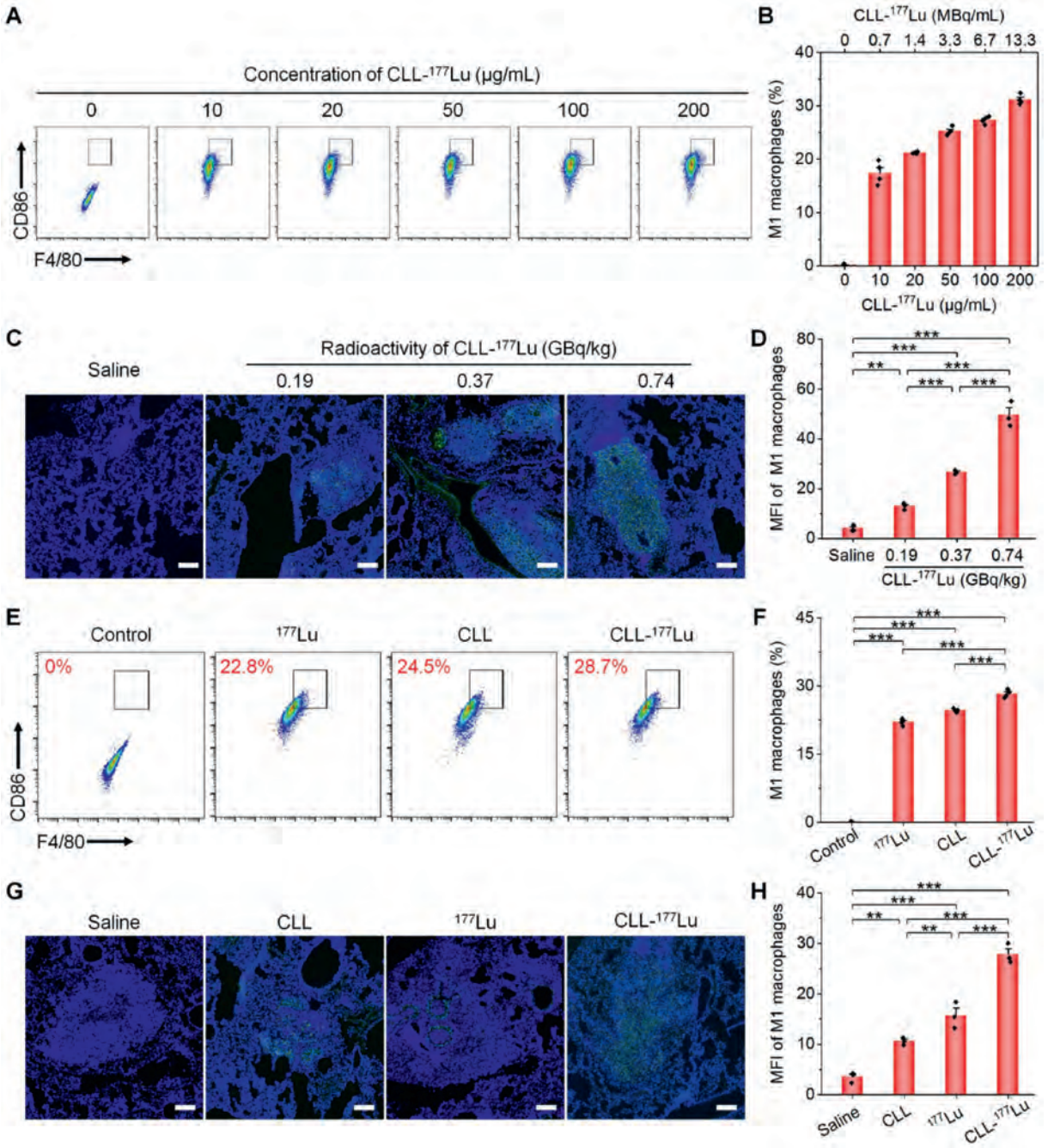


**Figure 5** CLL-$^{177}$Lu induces M1 polarization of macrophages *in vitro* and *in vivo*. (A, B) Flow cytometric profiles (A) and quantification (B) show *in vitro* M1 polarization of RAW264.7 macrophages after treatment with different doses of CLL-$^{177}$Lu. (C, D) Immunofluorescence images (C) and quantitative analysis (D) indicate relative counts of M1 macrophages in lungs after treatment with CLL-$^{177}$Lu. (E, F) Flow cytometric profiles (E) and quantification (F) show polarization of macrophages to the M1 phenotype following incubation with $^{177}$Lu, CLL, or CLL-$^{177}$Lu. (G, H) Immunofluorescence images (G) and quantitative analysis (H) of the relative counts of M1 macrophages in lungs after different treatments. Scale bars, 20 μm. Data are presented as means ± SD (B, F, $n = 4$; D, H, $n = 3$). $^{**}P < 0.01$, $^{***}P < 0.001$.

relatively high distributions of CLL-$^{177}$Lu in the liver, spleen, lungs, and kidneys (Fig. S14C−S14H). This tissue distribution pattern is consistent with those observed for other nanotherapies[61,62].

Moreover, both *in vivo* and *ex vivo* fluorescence imaging indicated a gradual accumulation of CLL-$^{177}$Lu in the tumors (Fig. S14I and S14J). Quantitative results suggested that CLL-$^{177}$Lu maintained relatively higher concentrations in tumors for at least 48 h (Fig. S14K). Together, these findings demonstrated that CLL-$^{177}$Lu may be eliminated from the body within 72 h. Since no targeting units are incorporated in CLL-$^{177}$Lu, its tumor accumulation is mainly attributed to passive targeting, which is dominated by the enhanced permeability and retention (EPR) effect, as well as endothelial cell-mediated active transport[63-65]. As well documented, both 4T1 and

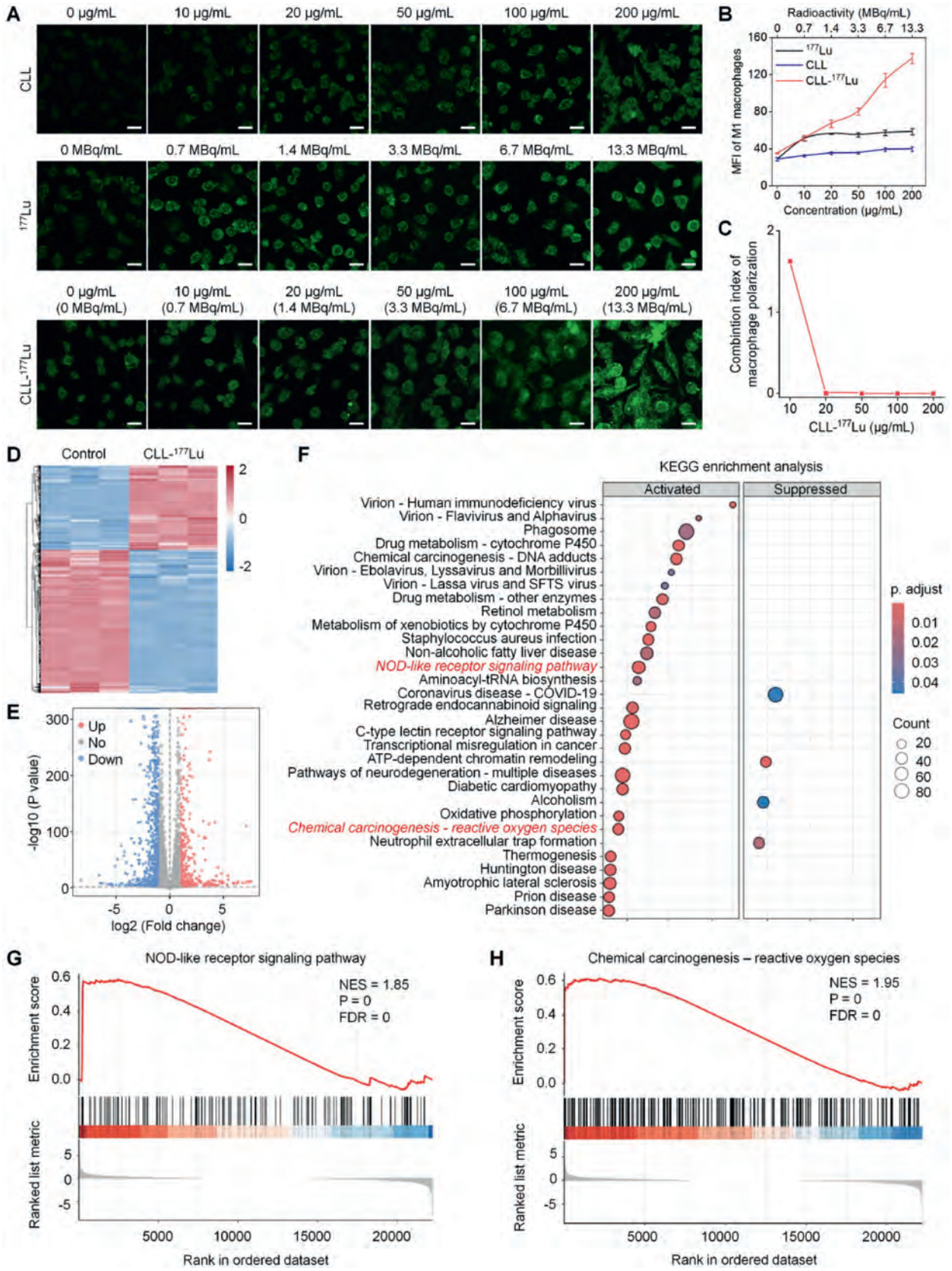


**Figure 6** Synergistic effects of CLL-$^{177}$Lu on the M1 polarization of macrophages and the underlying mechanisms. (A) CLSM images illustrate the dose-dependent ability of various doses of CLL, $^{177}$Lu, and CLL-$^{177}$Lu to induce M1 polarization of macrophages. Scale bars, 20 μm. (B) Quantified MFI values indicate relative counts of M1 macrophages after different treatments. (C) The calculated CI values demonstrate synergistic effects of CLL-$^{177}$Lu on macrophage M1 polarization in a dose-dependent manner. (D) Heatmap shows clustered DEGs

A549 tumors exhibit leaky vasculature[66-68], which can enhance the penetration of nanoparticles across the blood vessels.

### 3.8. *In vivo therapeutic effects of CLL-$^{177}$Lu in mice with subcutaneous xenograft tumors*

Following similar procedures, A549 tumor xenografts were established in nude mice. When the tumor volume was about 100 mm$^3$, mice were randomized into different groups that were injected with various doses of CLL-$^{177}$Lu twice *via* the tail vein, with an interval of 7 days (Supporting Information Fig. S15A). Monitoring the tumor volume during treatment indicated notable tumor growth in the model group treated with saline (Fig. S15B). Depending on the dosage, CLL-$^{177}$Lu therapy inhibited tumor growth. In particular, CLL-$^{177}$Lu at 0.37 and 0.74 GBq/kg dramatically inhibited tumor progression in mice during 12 days of treatment. Post treatment, tumors were isolated. Direction observation of isolated tumors and quantification showed that both the tumor volume and tumor weight were significantly reduced after treatment with different doses of CLL-$^{177}$Lu (Fig. S15C−S15E), compared to those of the model group. Consistent with the tumor inhibition effect, immunofluorescence analysis showed notably increased cell apoptosis in tumor sections, with a dose-dependent manner (Fig. S15F). Moreover, we observed significantly enhanced ROS levels and M1 macrophage proportions in three CLL-$^{177}$Lu groups (Fig. S15G and S15H). In all these cases, CLL-$^{177}$Lu at the examined highest dose of 0.74 GBq/kg exhibited the best therapeutic outcome. Collectively, these data demonstrated that CLL-$^{177}$Lu was also able to effectively inhibit the progression of lung cancer in a subcutaneous mouse xenograft model, largely by inducing ROS/$^1O_2$ generation and M1 polarization of macrophages. It is worth noting that CLL-$^{177}$Lu at 0.74 GBq/kg almost completely suppressed the tumor growth. This dose is only 1/10 of the clinically used therapeutic dose of $^{177}$Lu.

In a separate study, antitumor effects of CLL, $^{177}$Lu, and CLL-$^{177}$Lu at 0.37 GBq/kg were compared in mice bearing A549 tumor xenografts, following similar treatment procedures as above mentioned (Fig. 7A). The three examined formulations all inhibited the tumor volume increase, to varied degrees, as implicated by the tumor growth curves (Fig. 7B). After treatment, the CLL, $^{177}$Lu, and CLL-$^{177}$Lu groups exhibited significantly lower tumor volumes and tumor weights (Fig. 7C−E), compared to the saline group. Likewise, treatment with three therapies resulted in significantly increased cell apoptosis, ROS generation, and M1 macrophage subpopulation in tumor tissue sections (Fig. 7F−H). For all these aspects, CLL-$^{177}$Lu showed the most beneficial outcome.

Further, we compared antitumor effects of CLL-$^{177}$Lu at 0.37 GBq/kg with other formulations in mice bearing A549 xenograft tumors after a relatively long-term treatment period (Fig. 8A), which included CL, CLL, $^{177}$Lu, and L-$^{177}$Lu (*i.e.*, liposomes containing $^{177}$Lu alone). During and after 28 days of treatment, the CL group showed no significant inhibition of the tumor volume increase, compared to the model group (Fig. 8B and C). In contrast, interventions with CLL, $^{177}$Lu, or L-$^{177}$Lu significantly suppressed tumor growth. Analysis of the isolated tumors further verified that CLL and $^{177}$Lu-containing formulations more effectively reduced tumor weights, compared with CL (Fig. 8D and E). This is due to the non-specific distribution of CL after i.v. administration. Notably, CLL-$^{177}$Lu afforded the best outcomes, in terms of inhibiting tumor progression. Correspondingly, CLL-$^{177}$Lu most significantly induced cell apoptosis, enhanced ROS/$^1O_2$ production, and promoted M1 polarization of macrophages in tumor tissue sections (Fig. 8F−H). Moreover, immunofluorescence analysis of CD31 indicated that tumor angiogenesis was markedly attenuated after treatment with CLL, $^{177}$Lu, L-$^{177}$Lu, or CLL-$^{177}$Lu (Fig. 8I), with the most pronounced effect observed with CLL-$^{177}$Lu. These findings collectively confirmed the therapeutic advantages of CLL-$^{177}$Lu.

Subsequently, we interrogated whether CLL-$^{177}$Lu at 0.37 GBq/kg can inhibit lung metastasis of breast cancer in mice with 4T1 xenograft tumors (Fig. 9A). Over the course of 31 days of treatment, the CLL, $^{177}$Lu, L-$^{177}$Lu, and CLL-$^{177}$Lu groups exhibited significantly reduced tumor volumes, compared to the model group (Fig. 9B). Post-treatment, these groups also showed a marked reduction in tumor sizes and weights (Fig. 9C−E). Notably, CLL-$^{177}$Lu outperformed other therapies in suppressing tumor growth. More importantly, whereas lung metastasis was clearly observed in other groups through H&E-staining of lung tissues, as evidenced by the presence of pulmonary nodules and tumor cell infiltration, the CLL-$^{177}$Lu group exhibited negligible metastasis in the examined lung tissues (Fig. 9F). Supporting these favorable results, CLL-$^{177}$Lu therapy more effectively stimulated cell apoptosis, increased ROS/$^1O_2$ generation, induced M1 polarization of macrophages, and inhibited tumor angiogenesis, compared to the other formulations (Fig. 9G−J).

Collectively, the above findings demonstrated that our newly engineered ROS-triggerable PDT liposome CLL can also effectively inhibit the progression of lung cancer in a mouse xenograft model, by *in situ* mediating ROS/$^1O_2$ generation, increasing cell apoptosis, promoting M1 macrophage polarization, and inhibiting angiogenesis in the tumor microenvironment. By loading $^{177}$Lu into CLL, the finally developed dual-functional therapy CLL-$^{177}$Lu exhibited much better antitumor effects in mice bearing A549 or 4T1 tumor xenografts, largely resulting from synergistic effects of PDT, radiotherapy, and M1 macrophage-mediated immunotherapy. The potent tumor angiogenesis-inhibiting activity is another significant advantage for our newly developed combination therapy CLL-$^{177}$Lu.

### 3.9. *Safety evaluations of CLL-$^{177}$Lu*

Finally, safety profiles of CLL-$^{177}$Lu were tested. During the treatment of breast cancer lung metastasis in mice, animals in three therapeutic groups displayed normal body weight gains, with no significant difference compared to the saline-treated model group (Supporting Information Fig. S16A). After treatment, calculation of the organ index values of typical major organs revealed negligible changes in different groups (Fig. S16B). Furthermore, examination of H&E-stained pathological sections of major organs indicated no discernible destruction of tissue

based on transcriptomic analysis of RAW264.7 macrophages treated with fresh medium (Control) or CLL-$^{177}$Lu at 200 μg/mL. (E) A volcano plot illustrating DEGs between the control and CLL-$^{177}$Lu groups. (F) KEGG enrichment diagram indicates enriched pathways. (G, H) Gene set enrichment analysis (GSEA) shows the enriched NOD-like receptor signaling pathway (G) and pathways associated with ROS (H). Data in (B) are presented as means ± SD ($n = 3$).

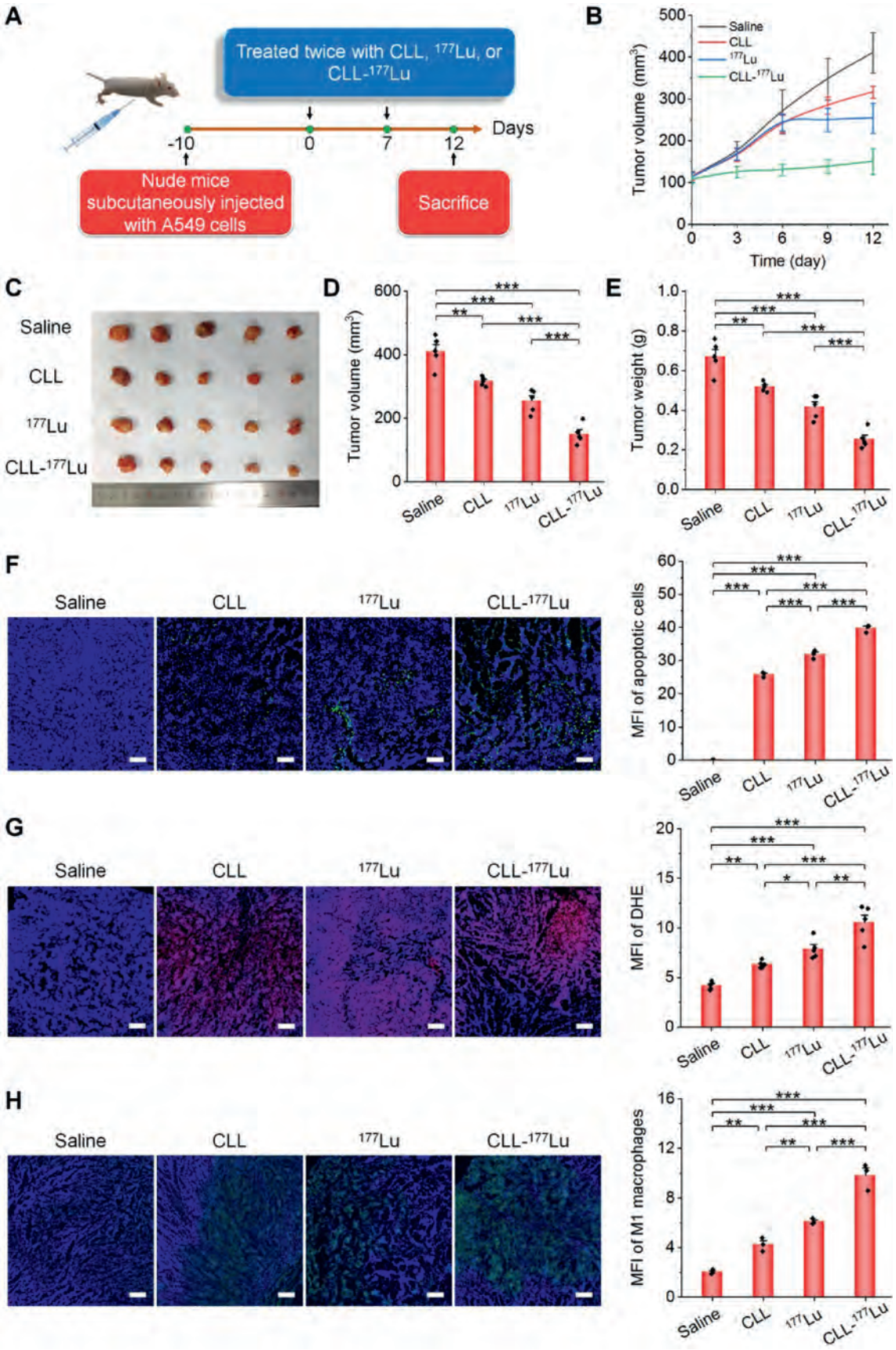


**Figure 7** Comparison of antitumor effects of $^{177}$Lu, CLL, and CLL-$^{177}$Lu in mice bearing A549 xenograft tumors. (A) A sketch illustrating treatment procedures. (B) Tumor growth curves during treatment with different formulations. (C–E) Digital photos (C) as well as quantified

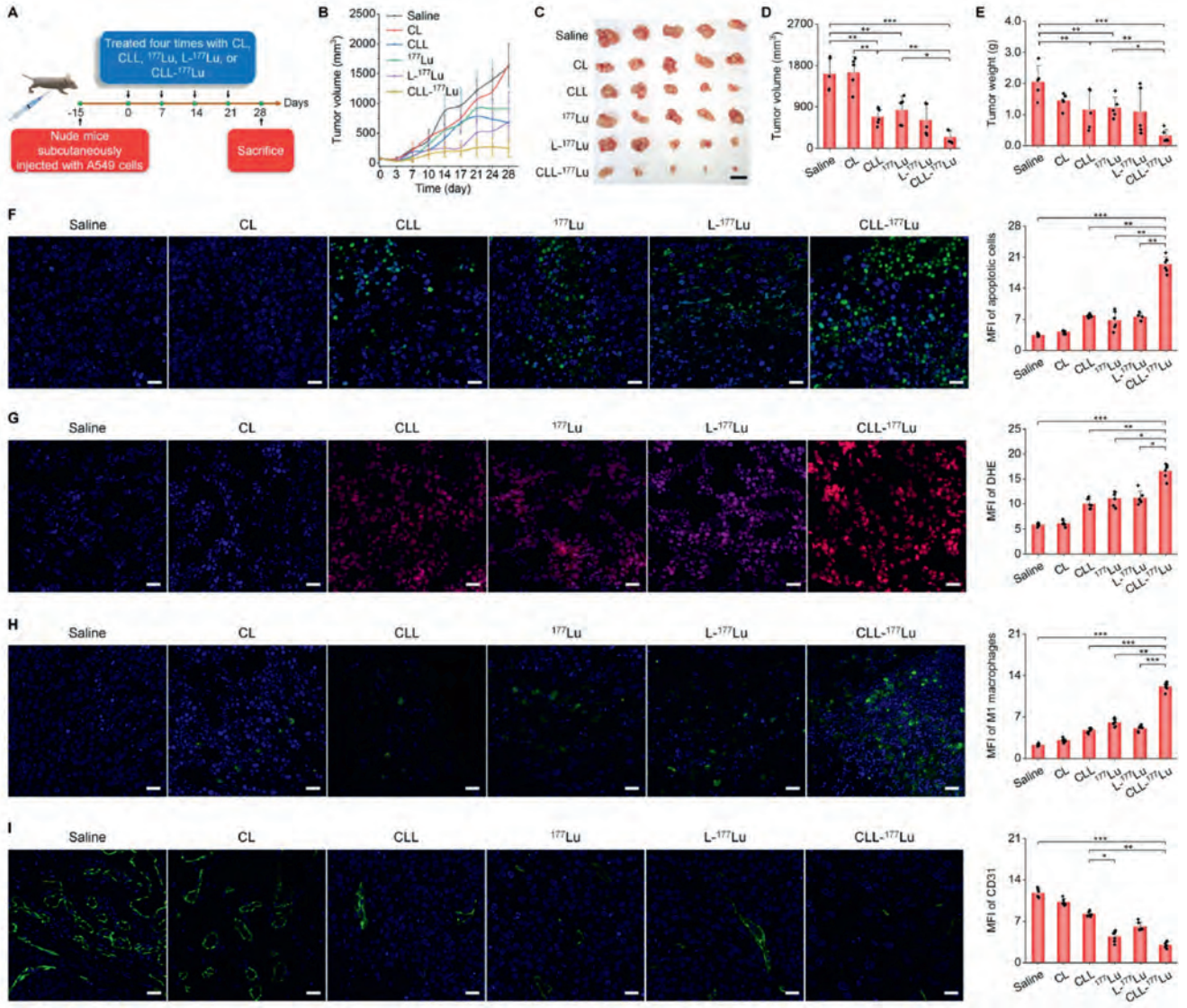


**Figure 8** Therapeutic effects of CLL-$^{177}$Lu in mice bearing A549 xenograft tumors after long-term treatment. (A) Schematic illustration of treatment protocols. CL, mice treated with 0.26 mg/kg CL; CLL, mice treated with 5 mg/kg CLL (equivalent to 0.26 mg/kg CL); $^{177}$Lu, mice treated with $^{177}$Lu at 0.37 GBq/kg; L-$^{177}$Lu, mice treated with L-$^{177}$Lu at 0.37 GBq/kg $^{177}$Lu; CLL-$^{177}$Lu, mice treated with CLL-$^{177}$Lu at 0.26 mg/kg CL and 0.37 GBq/kg $^{177}$Lu. (B) Changes in the tumor volume over a 28-day treatment period. (C) Digital photos of isolated tumors. Scale bar, 2 cm. (D, E) Quantified tumor volumes (D) and tumor weights (E) of isolated tumors post-treatment. (F) CLSM images (left) and quantitative analysis (right) of apoptotic cells in the tumor tissue sections following TUNEL staining. (G) CLSM images (left) and quantified MFI (right) indicate relative ROS levels in tumor tissue sections stained with DHE. (H) Immunofluorescence analysis of M1 macrophages in tumor tissues. (I) CLSM images and quantitative analysis of tumor angiogenesis by CD31 staining of tumor tissue sections. Scale bars, 20 μm. Data are presented as means ± SD (B, D, E, $n = 5$; F–I, $n = 6$). $^{*}P < 0.05$, $^{**}P < 0.01$, $^{***}P < 0.001$.

microstructure or infiltration of inflammatory cells (Fig. S16C). Additionally, measurement of representative biomarkers related to liver and kidney functions consistently showed no abnormal increases in serum levels of ALT, AST, CREA, and UREA, after treatment with CLL, $^{177}$Lu, and CLL-$^{177}$Lu (Supporting Information Fig. S17). Similar, during the treatment of mice with A549 xenograft tumors, the three examined therapies did not cause significant abnormalities in the body weight gain, organ index, tissue microstructures of major organs, and liver/kidney functions (Supporting Information Figs. S18 and S19). These results indicated that i.v. injection of CLL-$^{177}$Lu at 0.37 GBq/kg was safe in mice, even after repeated dosing regimens.

tumor volumes (D) and tumor weights (E) of isolated A549 tumors after different treatments. (F) Analysis of apoptotic cells in the tumor sections after TUNEL staining. (G) Analysis of relative ROS levels in tumor tissue sections after DHE staining. (H) Immunofluorescence analysis of M1 macrophages in tumor tissues. Scale bars, 20 μm. Data are presented as means ± SD (B, D, E, G, $n = 5$; F, H, $n = 3$). $^{*}P < 0.05$, $^{**}P < 0.01$, $^{***}P < 0.001$.

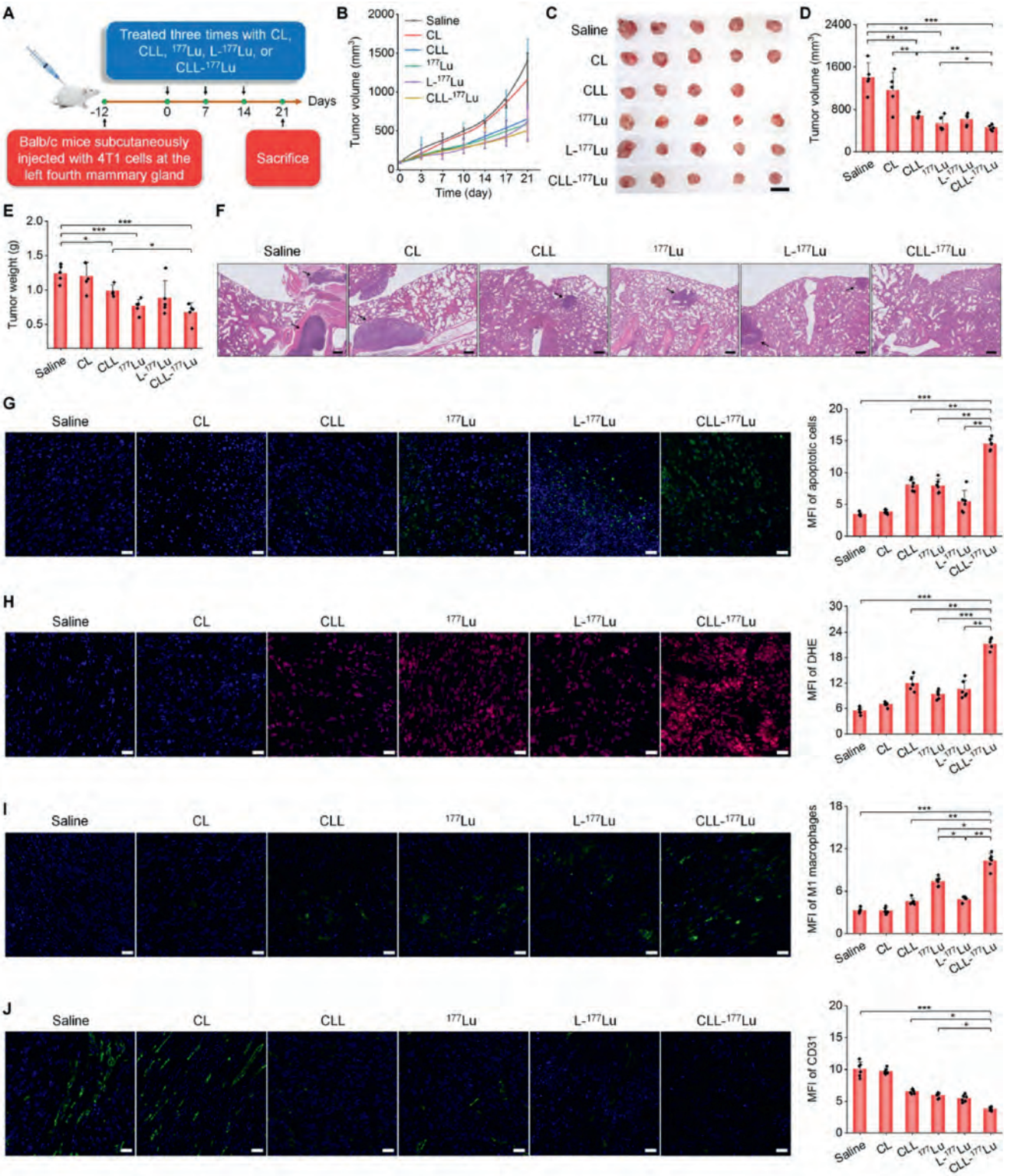


**Figure 9** *In vivo* antitumor effects of CLL-$^{177}$Lu in mice bearing 4T1 xenograft tumors. (A) A work flow shows treatment protocols. CL, 0.26 mg/kg; CLL, 5 mg/kg, equivalent to 0.26 mg/kg CL; $^{177}$Lu, 0.37 GBq/kg; L-$^{177}$Lu, 0.37 GBq/kg $^{177}$Lu; CLL-$^{177}$Lu, 0.26 mg/kg CL and 0.37 GBq/kg $^{177}$Lu. (B) Tumor volume changing profiles during a 21-day treatment period. (C) Digital photos of isolated tumors post-treatment. Scale bar, 2 cm. (D–E) Quantified tumor volumes (D) and tumor weights (E) of isolated tumors. (F) Microscopic images of H&E-stained lung sections following different treatments. (G) CLSM images (left) and quantitative analysis (right) of apoptotic cells in tumor sections after TUNEL staining. (H) Analysis of relative ROS levels in tumor tissue sections using DHE staining. (I) Immunofluorescence analysis of M1 macrophages in tumor tissues. (J) CLSM images (left) and quantitative analysis (right) of tumor angiogenesis in tumor tissue sections by CD31 staining. Scale bars: 100 μm (F); 20 μm (G–J). Data are presented as means ± SD (B, D, E, $n = 5$; G–J, $n = 6$). *$P < 0.05$, **$P < 0.01$, ***$P < 0.001$.

Moreover, we conducted safety studies of CLL-$^{177}$Lu in healthy BALB/c mice over a 32-day period. The animals were treated by i.v. injection of CLL-$^{177}$Lu at doses of 1.5 or 3.0 GBq/kg, which are 5 and 10 times higher than the dose of 0.37 GBq/kg used in therapeutic studies, respectively. While treatment with CLL-$^{177}$Lu at 3.0 GBq/kg resulted in animal death, beginning on Day 4 and culminating in the death of all mice in this group by Day 9, the mice treated with 1.5 GBq/kg CLL-$^{177}$Lu still exhibited body weight gain (Supporting Information Fig. S20A). On Day 32 after treatment, no significant changes in the organ index values of major organs (including the heart, liver, spleen, lung, and kidney) were observed in the 1.5 GBq/kg group (Fig. S20B). Similarly, we did not detect any abnormal increases in serum levels of biomarkers (ALT, AST, CREA, and UREA) relevant to liver and kidney functions for this group (Fig. S20C−S20F). Examination of H&E-stained tissue sections from the major organs revealed no discernible pathological alterations for mice treated with 1.5 GBq/kg (Fig. S20G). These preliminary results suggest that CLL-$^{177}$Lu is safe at doses below 1.5 GBq/kg. Nevertheless, further comprehensive studies are necessary to fully validate this issue.

## 4. Conclusions

In summary, we have developed a liposome therapy CLL-$^{177}$Lu with integrated *in situ* triggerable PDT and radiotherapy functions for targeted treatment of lung cancers. An *in situ* ROS-activatable photosensitizer CL was first synthesized by conjugating luminol with Ce6, which can be readily loaded into liposomes to give rise to an *in situ* ROS-triggerable liposome CLL for PDT treatment of tumors. CLL effectively induced ROS/$^1O_2$-generation in 4T1 and A549 tumor cells, thereby showing notable antitumor activity in a dose−response pattern. By packaging a radiopharmaceutical $^{177}$Lu into the ROS-activatable PDT liposome, a dual-functional nanotherapy CLL-$^{177}$Lu was engineered, enabling simultaneous PDT and radiotherapy. CLL-$^{177}$Lu demonstrated synergistic antitumor effects in both 4T1 and A549 tumor cells, showing stronger efficacy than CLL. Correspondingly, CLL-$^{177}$Lu effectively inhibited tumor progression in a mouse model of 4T1 breast cancer lung metastasis and mice bearing A549 tumor xenografts. In addition to inducing ROS/$^1O_2$ production and promoting tumor cell apoptosis, the combination of PDT and radiotherapy in CLL-$^{177}$Lu remarkably increased M1 polarization of macrophages, thus facilitating M1 macrophage-mediated immunotherapy. Importantly, the tumor angiogenesis-inhibiting activity is a distinctive feature of our combination liposome therapy, which is highly advantageous for suppressing tumor metastasis. Furthermore, preliminary studies revealed good safety of CLL-$^{177}$Lu after i.v. injection at therapeutic doses. Consequently, our dual-functional liposome CLL-$^{177}$Lu is a promising nanotherapy for cancer treatment. Moreover, in view of the powerful loading capacity of liposomes to different types of drugs, the PDT liposome CLL can be used for delivering various therapies to achieve synergistic antitumor effects.

## Acknowledgments

This study was supported by National Natural Science Foundation of Chongqing (No. CSTB2022NSCQ-MSX0150), the New Chongqing Youth Innovative Talent Program (No. CSTB 2024NSCQ-QCXMX0005), the National Natural Science Foundation of China (No. 81801841), and the Graduate Supervisor Team Program of Chongqing in 2022.

## Author contribution

Chunsen Yuan: Writing − original draft, Investigation, Methodology. Taotao Jin: Investigation. Hangke Lei: Methodology, Investigation. Juanjuan Liu: Investigation. Wendan Pu: Investigation, Writing − original draft. Yang Zhang: Investigation. Chenwen Li: Investigation. Dingde Huang: Supervision, Funding acquisition, Writing − review & editing, Project administration. Jianxiang Zhang: Funding acquisition, Writing − review & editing, Conceptualization, Project administration, Supervision. Jiawei Guo: Writing − original draft, Funding acquisition, Writing − review & editing, Supervision, Project administration.

## Conflicts of interest

The authors have no conflicts of interest to declare.

## Appendix A. Supporting information

Supporting information to this article can be found online at https://doi.org/10.1016/j.apsb.2025.06.026.

## References

1. Leiter A, Veluswamy RR, Wisnivesky JP. The global burden of lung cancer: current status and future trends. *Nat Rev Clin Oncol* 2023;**20**:624−39.
2. Kondo KK, Rahman B, Ayers CK, Relevo R, Griffin JC, Halpern MT. Lung cancer diagnosis and mortality beyond 15 years since quit in individuals with a 20+ pack-year history: a systematic review. *CA Cancer J Clin* 2024;**74**:84−114.
3. Megyesfalvi Z, Gay CM, Popper H, Pirker R, Ostoros G, Heeke S, et al. Clinical insights into small cell lung cancer: tumor heterogeneity, diagnosis, therapy, and future directions. *CA Cancer J Clin* 2023;**73**:620−52.
4. Li YT, Yan BS, He SM. Advances and challenges in the treatment of lung cancer. *Biomed Pharmacother* 2023;**169**:115891.
5. Li YH, Liu XH, Zhang X, Pan W, Li N, Tang B. Immune cycle-based strategies for cancer immunotherapy. *Adv Funct Mater* 2021;**31**:2107540.
6. Rosenblum D, Joshi N, Tao W, Karp JM, Peer D. Progress and challenges towards targeted delivery of cancer therapeutics. *Nat Commun* 2018;**9**:1410.
7. Sun W, Zhang Q, Wang X, Jin Z, Cheng Y, Wang GF. Clinical practice of photodynamic therapy for non-small cell lung cancer in different scenarios: who is the better candidate?. *Respiration* 2024;**103**:193−204.
8. Verma J, Warsame C, Seenivasagam RK, Katiyar NK, Aleem E, Goel S. Nanoparticle-mediated cancer cell therapy: basic science to clinical applications. *Cancer Metastasis Rev* 2023;**42**:601−27.
9. Yu Q, Li X, Wang J, Guo LP, Gao WY, Huang LQ. Recent advances in reprogramming strategy of tumor microenvironment for rejuvenating photosensitizers-mediated photodynamic therapy. *Small* 2024;**20**:e2305708.
10. Wang YC, Staudinger JN, Mindt TL, Gasser G. Theranostics with photodynamic therapy for personalized medicine: to see and to treat. *Theranostics* 2023;**13**:5501−44.
11. Zheng YL, Ye JX, Li ZY, Chen HJ, Gao Y. Recent progress in sonophotodynamic cancer therapy: from developed new sensitizers to nanotechnology-based efficacy-enhancing strategies. *Acta Pharm Sin B* 2021;**11**:2197−219.

12. Li X, Lovell JF, Yoon J, Chen X. Clinical development and potential of photothermal and photodynamic therapies for cancer. *Nat Rev Clin Oncol* 2020;**17**:657−74.
13. Liu QF, Qian YY, Li PL, Zhang SH, Wang ZR, Liu JJ, et al. The combined therapeutic effects of $^{131}$iodine-labeled multifunctional copper sulfide-loaded microspheres in treating breast cancer. *Acta Pharm Sin B* 2018;**8**:371−80.
14. Kim YR, Kim S, Choi JW, Choi SY, Lee SH, Kim H, et al. Bioluminescence-activated deep-tissue photodynamic therapy of cancer. *Theranostics* 2015;**5**:805−17.
15. Kang JS, Jeong H, Jeong M, Kim J, Park S, Jung JY, et al. *In situ* activatable nitrobenzene-cysteine-copper(II) nano-complexes for programmed photodynamic cancer therapy. *J Am Chem Soc* 2023;**145**:27587−600.
16. Obaid G, Celli JP, Broekgaarden M, Bulin A-L, Uusimaa P, Pogue B, et al. Engineering photodynamics for treatment, priming and imaging. *Nat Rev Bioeng* 2024;**2**:1−18.
17. Kaae J, Philipsen PA, Haedersdal M, Wulf HC. Immediate whealing urticaria in red light exposed areas during photodynamic therapy. *Acta Derm Venereol* 2008;**88**:480−3.
18. Blum NT, Zhang YF, Qu JL, Lin J, Huang P. Recent advances in self-exciting photodynamic therapy. *Front Bioeng Biotechnol* 2020;**8**:594491.
19. Yang YK, Hou WY, Liu SY, Sun K, Li MY, Wu CF. Biodegradable polymer nanoparticles for photodynamic therapy by bioluminescence resonance energy transfer. *Biomacromolecules* 2018;**19**:201−8.
20. Kamkaew A, Cheng L, Goel S, Valdovinos HF, Barnhart TE, Liu Z, et al. Cerenkov radiation induced photodynamic therapy using chlorin e6-loaded hollow mesoporous silica nanoparticles. *Acs Appl Mater Inter* 2016;**8**:26630−7.
21. Chen TC, Huang L, Liu CC, Chao PJ, Lin FH. Luminol as the light source for photodynamic therapy. *Process Biochem* 2012;**47**:1903−8.
22. Xu X, An H, Zhang D, Tao H, Dou Y, Li X, et al. A self-illuminating nanoparticle for inflammation imaging and cancer therapy. *Sci Adv* 2019;**5**:eaat2953.
23. de Santana WMOS, Surur AK, Momesso VM, Lopes PM, Santilli CV, Fontana CR. Nanocarriers for photodynamic-gene therapy. *Photodiagnosis Photodyn Ther* 2023;**43**:103644.
24. Sun Q, Hong ZY, Zhang C, Wang LL, Han ZQ, Ma D. Immune checkpoint therapy for solid tumours: clinical dilemmas and future trends. *Signal Transduct Targeted Ther* 2023;**8**:320.
25. Lang X, Wang X, Han M, Guo Y. Nanoparticle-mediated synergistic chemoimmunotherapy for cancer treatment. *Int J Nanomed* 2024;**19**:4533−68.
26. Chen JJ, Yuan F, Zheng LY, Wen LL, Gao M, Zhou WM, et al. Limitations of ALA-PDT as a reliable therapy for AK in clinical practice. *Photodiagnosis Photodyn Ther* 2023;**44**:103797.
27. Yu L, Wang ZJ, Mo ZM, Zou BH, Yang YY, Sun R, et al. Synergetic delivery of triptolide and Ce6 with light-activatable liposomes for efficient hepatocellular carcinoma therapy. *Acta Pharm Sin B* 2021;**11**:2004−15.
28. Chen YN, Zhou QQ, Jia ZF, Cheng N, Zhang S, Chen WD, et al. Enhancing cancer immunotherapy: nanotechnology-mediated immunotherapy overcoming immunosuppression. *Acta Pharm Sin B* 2024;**14**:3834−54.
29. Morton CA, Szeimies RM, Braathen LR. Review of the european society for photodynamic therapy (Euro-PDT) annual congress 2022. *Eur J Dermatol* 2023;**33**:467−73.
30. Lam WC, Choudhry N, Wong D. Polypoidal choroidal vasculopathy in Canada. *Can J Opthalmol J Can Opthalmol* 2020;**55**:199−211.
31. Duan XP, Chan C, Guo NN, Han WB, Weichselbaum RR, Lin WB. Photodynamic therapy mediated by nontoxic core−shell nanoparticles synergizes with immune checkpoint blockade to elicit antitumor immunity and antimetastatic effect on breast cancer. *J Am Chem Soc* 2016;**138**:16686−95.
32. Chen HM, Wang GD, Chuang YJ, Zhen ZP, Chen XY, Biddinger P, et al. Nanoscintillator-mediated X-ray inducible photodynamic therapy for *in vivo* cancer treatment. *Nano Lett* 2015;**15**:2249−56.
33. Lioret V, Bellaye PS, Bernhard Y, Moreau M, Guillemin M, Drouet C, et al. Cherenkov Radiation induced photodynamic therapy—repurposing older photosensitizers, and radionuclides. *Photodiagnosis Photodyn Ther* 2023;**44**:103816.
34. Cuadrado CF, Lagos KJ, Stringasci MD, Bagnato VS, Romero MP. Clinical and pre-clinical advances in the PDT/PTT strategy for diagnosis and treatment of cancer. *Photodiagnosis Photodyn Ther* 2024;**50**:104387.
35. Sun N, Wang T, Zhang S. Radionuclide-labelled nanoparticles for cancer combination therapy: a review. *J Nanobiotechnol* 2024;**22**:728.
36. Wang P, Wang B, Zhang L, Liu X, Shi L, Kang X, et al. Clinical practice guidelines for 5-aminolevulinic acid photodynamic therapy for acne vulgaris in China. *Photodiagnosis Photodyn Ther* 2023;**41**:103261.
37. Sun W, Luo L, Feng Y, Qiu Y, Shi C, Meng S, et al. Gadolinium-rose bengal coordination polymer nanodots for MR-/fluorescence-image-guided radiation and photodynamic therapy. *Adv Mater* 2020;**32**:e2000377.
38. Kotagiri N, Sudlow GP, Akers WJ, Achilefu S. Breaking the depth dependency of phototherapy with Cerenkov radiation and low-radiance-responsive nanophotosensitizers. *Nat Nanotechnol* 2015;**10**:370−9.
39. Fang L, Huang H, Quirk JD, Zheng J, Shen D, Manion B, et al. Analysis of stable chelate-free gadolinium loaded titanium dioxide nanoparticles for MRI-guided radionuclide stimulated cancer treatment. *Curr Anal Chem* 2022;**18**:826−35.
40. Allison RR, Bansal S. Photodynamic therapy for peripheral lung cancer. *Photodiagnosis Photodyn Ther* 2022;**38**:102825.
41. Khakwani A, Harden S, Beckett P, Baldwin D, Navani N, West D, et al. Post-treatment survival difference between lobectomy and stereotactic ablative radiotherapy in stage I non-small cell lung cancer in England. *Thorax* 2020;**75**:237−43.
42. Qian RJ, Wang K, Guo YW, Li HY, Zhu ZY, Huang XJ, et al. Minimizing adverse effects of Cerenkov radiation induced photodynamic therapy with transformable photosensitizer-loaded nanovesicles. *J Nanobiotechnol* 2022;**20**:203.
43. Zhang J, Zhao T, Jakobsson V, Chen X. Clinical translation of radiotheranostics for precision oncology. *Nat Rev Bioeng* 2023;**1**:612−4.
44. Giunta EF, Brighi N, Gurioli G, Matteucci F, Paganelli G, De Giorgi U. $^{177}$Lu-PSMA therapy in metastatic prostate cancer: an updated review of prognostic and predictive biomarkers. *Cancer Treat Rev* 2024;**125**:102699.
45. George SC, Samuel EJJ. Developments in $^{177}$Lu-based radiopharmaceutical therapy and dosimetry. *Front Chem* 2023;**11**:1218670.
46. Li HM, Xu TT, Hua QC, Wang L, Chen Y. $^{177}$Lu-DOTA-IBA therapy in prostate cancer with bone metastases. *Clin Nucl Med* 2023;**48**:740−2.
47. Watanabe S, Hashimoto K, Ishioka NS. Lutetium-177 complexation of DOTA and DTPA in the presence of competing metals. *J Radioanal Nucl Chem* 2015;**303**:1519−21.
48. Zhang B, Jiang T, She XJ, Shen S, Wang S, Deng J, et al. Fibrin degradation by rtPA enhances the delivery of nanotherapeutics to A549 tumors in nude mice. *Biomaterials* 2016;**96**:63−71.
49. He SQ, Wang LL, Wu DX, Tong F, Zhao H, Li HM, et al. Dual-responsive supramolecular photodynamic nanomedicine with activatable immunomodulation for enhanced antitumor therapy. *Acta Pharm Sin B* 2024;**14**:765−80.
50. Zheng HW, Yuan CS, Cai JJ, Pu WD, Wu P, Li CW, et al. Early diagnosis of breast cancer lung metastasis by nanoprobe-based luminescence imaging of the pre-metastatic niche. *J Nanobiotechnol* 2022;**20**:134.
51. Cui X, Li X, Peng C, Qiu YH, Shi Y, Liu YM, et al. Beyond external light: on-spot light generation or light delivery for highly penetrated photodynamic therapy. *ACS Nano* 2023;**17**:20776−803.
52. Foglietta F, Serpe L, Canaparo R. ROS-generating nanoplatforms as selective and tunable therapeutic weapons against cancer. *Discov Nano* 2023;**18**:151.
53. Du JJ, Shi TC, Long SR, Chen PZ, Sun W, Fan JL, et al. Enhanced photodynamic therapy for overcoming tumor hypoxia: from microenvironment regulation to photosensitizer innovation. *Coord Chem Rev* 2021;**427**:213604.

54. Sun AL, Mu WW, Li YM, Sun YL, Li PX, Liu RM, et al. Piperlongumine analogs promote A549 cell apoptosis through enhancing ROS generation. *Molecules* 2021;**26**:3243.
55. Viola-Villegas N, Doyle RP. The coordination chemistry of 1,4,7,10−tetraazacyclododecane−*N,N′,N″,N‴*−tetraacetic acid (H4DOTA): structural overview and analyses on structure-stability relationships. *Coord Chem Rev* 2009;**253**:1906−25.
56. Arbuznikova D, Eder M, Grosu AL, Meyer PT, Gratzke C, Zamboglou C, et al. Towards improving the efficacy of PSMA-targeting radionuclide therapy for late-stage prostate cancer-combination strategies. *Curr Oncol Rep* 2023;**25**:1363−74.
57. Siwowska K, Guzik P, Domnanich KA, Monne Rodriguez JM, Bernhardt P, Ponsard B, et al. Therapeutic potential of $^{47}$Sc in comparison to $^{177}$Lu and $^{90}$Y: preclinical investigations. *Pharmaceutics* 2019;**11**:424.
58. Xiang XN, Wang JG, Lu D, Xu X. Targeting tumor-associated macrophages to synergize tumor immunotherapy. *Signal Transduct Targeted Ther* 2021;**6**:75.
59. Xu H, Xiong S, Chen Y, Ye Q, Guan N, Hu Y, et al. Flagella of tumor-targeting bacteria trigger local hemorrhage to reprogram tumor-associated macrophages for improved antitumor therapy. *Adv Mater* 2023;**35**:e2303357.
60. Liu Y, Wang Y, Wang C, Dong T, Xu H, Guo Y, et al. Hijacking self-assembly to establish intracellular functional nanoparticles. *Adv Sci* 2022;**9**:e2203027.
61. Mukherjee S, Joshi V, Reddy KP, Singh N, Das P, Datta P. Biopharmaceutical and pharmacokinetic attributes to drive nanoformulations of small molecule tyrosine kinase inhibitors. *Asian J Pharm Sci* 2024; **19**:100980.
62. Li XT, Chen L, Huang MT, Zeng ST, Zheng JY, Peng SY, et al. Innovative strategies for photodynamic therapy against hypoxic tumor. *Asian J Pharm Sci* 2023;**18**:100775.
63. Nichols JW, Bae YH. EPR: evidence and fallacy. *J Control Release* 2014;**190**:451−64.
64. Wilhelm S, Tavares AJ, Dai Q, Ohta S, Audet J, Dvorak HF, et al. Analysis of nanoparticle delivery to tumours. *Nat Rev Mater* 2016;**1**:16014.
65. Sindhwani S, Syed AM, Ngai J, Kingston BR, Maiorino L, Rothschild J, et al. The entry of nanoparticles into solid tumours. *Nat Mater* 2020;**19**:566−75.
66. Naumenko VA, Vlasova KY, Garanina AS, Melnikov PA, Potashnikova DM, Vishnevskiy DA, et al. Extravasating neutrophils open vascular barrier and improve liposomes delivery to tumors. *ACS Nano* 2019;**13**:12599−612.
67. Liu Z, Zhang Y, Shen N, Sun J, Tang Z, Chen X. Destruction of tumor vasculature by vascular disrupting agents in overcoming the limitation of EPR effect. *Adv Drug Deliv Rev* 2022;**183**:114138.
68. Izci M, Maksoudian C, Manshian BB, Soenen SJ. The use of alternative strategies for enhanced nanoparticle delivery to solid tumors. *Chem Rev* 2021;**121**:1746−803.